AD-A163 955

DTIC
ELECTE
FEB 1 3 1986
S   D
R
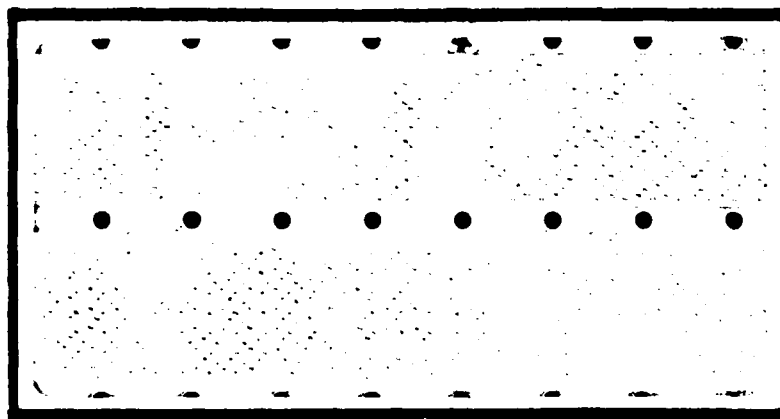
DEPARTMENT OF THE AIR FORCE

AIR UNIVERSITY

AIR FORCE INSTITUTE OF TECHNOLOGY

Wright-Patterson Air Force Base, Ohio

86 2 3

AFIT/GEP/ENP/85D-5

DTIC
ELECTED
S FEB 1 3 1986
D

THE CONSTRUCTION AND CALIBRATION OF A

LADAR CROSS-SECTION MEASUREMENT RANGE

THESIS

James C. Higgins
Captain, USAF

AFIT/GEP/ENP/85D-5

AFIT/GEP/ENP/85D-5

THE CONSTRUCTION AND CALIBRATION OF A

LADAR CROSS-SECTION MEASUREMENT RANGE

THESIS

Presented to the Faculty of the School of Engineering

of the Air Force Institute of Technology

Air University

In Partial Fulfillment of the

Requirements for the Degree of

Master of Science in Engineering Physics

James C. Higgins, B.S.

Captain, USAF

December 1985

Approved for public release; distribution unlimited

Preface

It is with great joy and much delight that I am finally completing this effort with these last few words. This research has been a tremendous learning experience, and for that reason, I value it. I do hope, though, that the work contained within this document proves useful to someone else. When that is the case, the total effort assumes additional significance because of the value others place in it.

My wife, Kathy, has been a blessing to me. When I grew up, I never envisioned starting my marriage by going back to school, yet alone to AFIT, where free time is a luxury. Kathy has supported me through it all, and I wish to dedicate this, and my love, to her.

The experiment would have taken much longer were it not for Ron Gabriel who consistently helped me find the equipment I needed. In addition, my good friend, Joe Gribble, provided valuable suggestions on how to improve this document. My sincere thanks to both.

Finally, I wish to thank my advisor, Maj. Jim Mills, who has provided me with important guidance and encouragement ever since I first entered the service 5 years ago.

J. C. Higgins

Table of Contents

List of Figures

List of Tables

AFIT/GEP/ENP/85D-5

Abstract

This research effort measured the size of the optical signals
scattered by highly specular spheres when illuminated by plane
wavefronts. This was repeated for 13 different sized spheres so that
the functional dependency on sphere size could be more accurately
established. The experiment was conducted at $\lambda = 1.064 \mu m$ and at a
fixed range of 731.5 cm in a bistatic configuration.

An analytical development based on geometric optics was used to
predict the results. Within the limits of the small angle
approximations, the results were generally within 10% of the measured
values. The surface quality of the spheres and the alignment of the
experiment were found to be the most critical variables affecting
accuracy.

THE CONSTRUCTION AND CALIBRATION OF A
LADAR CROSS-SECTION MEASUREMENT RANGE

I. Introduction

The purpose of this ~~research~~ *th...* was to construct an experiment that can accurately determine a target's laser radar cross-section. A "laser radar cross-section" (LRCS) is a measure of the average amount of optical power scattered by a target, and is analogous to the term "radar cross-section" ~~(RCS)~~, which is defined for scattered power radiating at microwave wavelengths. Cross-sections, whether optical or microwave, are quantities which describe the effective area of a specific target which directly scatters an incident electromagnetic (EM) wavefront. The focus of this thesis is to investigate the nature of LRCS measurements, with particular attention paid to the measurements of spherical calibration targets.

~~Background~~

RAdio Detection And Ranging (RADAR) devices are probably the best known of all man-made active detection systems. They are members of a larger group known as remote sensors, which include systems either man-made or biological, active or passive, and finally, electromagnetic or ultrasonic. Remote sensors are sensitive tools which can detect a signal, traveling freely through a medium, whose source is some finite distance away. These sensors are considered "passive" if their supporting systems don't illuminate the target. Instead, passive sensors detect emissions and reflections that are characteristic of the target;

1

the human eye is an example of a passive detector. By contrast, active sensors transmit a particular type of waveform, and then detect and interpret that small part of the reflected signal which returns. Radar and sonar (SOund NAvigation and Ranging) systems are examples of active detection schemes.

Radar. Radar devices were one of the more significant consequences of investigations into the response which specific materials had to an incident EM field (Skolnik, 1962:8-10). These scattering and diffraction studies eventually centered around the microwave frequencies which are now characteristic of radar devices. The notion of a scattering cross-section developed from these studies, and can be defined in fundamental terms as the ratio of the power scattered, per unit solid angle, divided by the incident flux (AFAL-TR-75-116:3). It is a function of many parameters, among which are the reflectivity at microwave wavelengths and the size, shape, and texture of the reflecting surface. The RCS parameter has the dimensions of area, and can be expressed by

$$\sigma_R = \frac{(\text{POWER REFLECTED TOWARDS SOURCE} \ / \ \text{UNIT SOLID ANGLE})}{(\text{INCIDENT POWER DENSITY} \ / \ 4\pi)} \tag{1}$$

For all but the most symmetric targets (i.e., a sphere or a flat plate), the cross-section does not bear a simple relationship to the physical surface area, except that the larger a target is, the greater the cross-section is likely to be. The significance of cross-section is directly tied to its linear relationship with the power of the return signal captured by the radar system's receiving antenna:

2

$$P_r \text{ (radar)} = \frac{P_t\, G_t\, A}{(4\pi R^2)^2}\, \sigma_R \tag{2}$$

(not accounting for atmospheric attenuation)

where

P_r = return signal power (detected by the radar)
P_t = radiated signal power (at the output of the device)
G_t = power gain due to the antenna's directionality
A = effective capture area of the antenna

Eq (2) is the primary form of the radar range equation, the importance of which lies in its ability to describe the maximum radar range at which a target can just be detected. This R_{max} can be calculated when the minimum value of P_r is known for the detector system (Skolnik, 1962:4).

Laser Radar. With the introduction of the laser in 1960, it became possible to apply the fundamentals of radar theory to the optical regime of the EM spectrum. The end product was a laser radar, which illuminates the target with a coherent, monochromatic beam of light and then, like its microwave predecessor, detects the scattered return signal. Using Bachman's definitions, laser radar will now be referred to as "LADAR" (LAser Detection And Ranging) (Bachman, 1979:2). Ladar systems currently being researched include those operating at $10.59\mu m$ and at $1.06\mu m$ (i.e., those with CO_2 and Nd:YAG laser sources, respectively). Much like its radar counterpart, there is a LRCS associated with every target, and it can be expressed by

$$\sigma_L = \frac{(POWER\ REFLECTED\ TOWARDS\ SOURCE\ /\ RETURN\ SOLID\ ANGLE)}{(INCIDENT\ POWER\ DENSITY\ /\ TOTAL\ RERADIATED\ SOLID\ ANGLE)} \tag{3}$$

3

Likewise, the power captured by the ladar system's receiving optics is described by

$$P_r \text{ (ladar)} = \frac{P_t A_c}{\Omega_i \, \Omega_r \, R^4} \, \sigma_L \tag{4}$$

(not accounting for atmospheric attenuation)

where

P_r = return signal power (detected by the ladar)
P_t = radiated signal power (at the output of the device)
Ω_i = incident solid angle (measured from the ladar to the target)
Ω_r = receiver solid angle (measured from the target to the ladar)
A_c = receiver clear aperture area

(Bachman, 1979:9-10). This is the primary form of the ladar range equation, which, like the radar range equation, provides important information for the definition of the maximum ladar range at which a target can be detected.

Significance of Range Equations. The previous equations provide much insight into the effect that various parameters, including a target's optical and microwave cross-sections, have upon the performance of both ladar and radar systems. The engineers who design these two types of systems can control, to some extent, all of the variables, except for the target's cross-section. Even the varying effects of the atmosphere can be somewhat compensated for. If, in fact, all of the other parameters in these two equations were equal, range performance at any particular wavelength would depend only on the target's cross-section at that wavelength. For this simplified scenario, a comparison of these cross-sections would be very important to the U.S. Air Force. Success in the ongoing effort to significantly reduce a target's radar

cross-section may not have a proportional effect on its optical cross-section. There is reason to believe that a target's LRCS may remain unchanged, or even grow larger, as its RCS is reduced. Open source publications (unclassified) have stated that "the Lockheed SR-71 Black-bird, a forerunner in the application of 'stealth' technologies, has been known to become visible to the unaided eye before becoming visible on radar" (Schefter, 1983:61). If this "visibility" also exists at a useful laser wavelength, then ladar systems may detect hostile targets at ranges much greater than their microwave counterparts are capable of. Furthermore, this information would be significant in the evaluation of future designs of out nation's own stealth aircraft.

Thesis Objective

The primary objective of this entire effort was to design and build an experiment capable of quantitatively measuring a target's LRCS. Since the definition of cross-section, as seen at optical wavelengths, is not presently standardized within the scientific community, a clear definition was chosen. The first of three specific goals involved the theoretical examination of the LRCS to be expected from a highly reflecting sphere. This investigation examined the backscattered return signal from such spheres in terms of both geometric optics and wave optics; furthermore, an attempt has been made to predict, using geomet-ric optics, the actual size of the signal expected in a laboratory measurement. The second goal comprised the construction, refinement, and execution of an experiment (using a pulsed Nd:YAG laser at $1.064 \mu m$) which can reliably measure a specific target's LRCS at normal incidence. The usefulness of this LRCS Measurement Range depended greatly on a

proper prior evaluation and control of experimental errors. The final goal actually consisted of making LRCS measurements of high quality spheres and then comparing these results with the predictions made by the geometric optics model.

Scope

This thesis effort was limited to considerations of only optical cross-section measurements which are a function of the spherical target's radius, alignment, and range. The geometry of a target usually plays a very important and complicated role in these measurements; spherical shapes, however, have no preferred orientation provided that the substance is optically isotropic. This makes the sphere an ideal geometry for the investigation of LRCS measurements. The design of the experiment dictates that all targets will each be measured at the same position, a distance of 7.3 meters from a known reference point on the experimental table and along the laser's optic axis. All the measurements were conducted in the laser's far field, and the assumption was made that careful control of the experiment could ensure that the targets were overfilled by plane waves of constant irradiance.

Atmospheric attenuation is a serious problem in quantifying the performance of an operational LADAR system. Its effects, however, were not considered in this research; furthermore, they were literally calibrated out of the experiment before each LRCS measurement was made.

General Approach

The second thesis goal that is stated on pg 5 involves construction of a working laser radar cross-section measurement range. Chapter II discusses the organization and layout of such a range. The individual

components of the experiment are described, and in some cases, justified. The emphasis is on the impact that certain design considerations have on the quality of the data obtained.

Chapter III addresses the theory of laser pulse scattering from a highly reflective spherical target. A model of the interaction is described, in terms of geometrical optics, and then predictions of the experimental results are made. These numeric predictions are tabulated in Appendix B. Finally, a model based on physical optics is recommended. A reference is made to Appendix C where a detailed but incomplete model of the experiment, using the Huygens-Fresnel theory, is presented.

The techniques used to prepare and properly conduct the experiment are presented in Chapter IV. The alignment process will be reviewed, but not covered in detail. Attention is focused primarily on the problems unique to the experiment, the control of errors, and the subtle pitfalls to be avoided.

In Chapter V, the experimental measurements are presented and then analyzed in terms of the geometric theory developed in Chapter III.

Conclusions and recommendations are offered in Chapter VI. An appraisal of specular spheres as LRCS Calibration Standards is made. Finally, recommendations for future study are presented with emphasis on problems relating to the collection of accurate LRCS data.

II. EXPERIMENTAL SETUP

The experimental measurement of the LRCS of many targets is of
significant importance. The optical properties of some radically new
materials cannot be accurately predicted based on theoretical calcu-
lations alone. With a need for precise knowledge of LRCS signatures,
let us now consider what is required in terms of equipment, and its
performance, in order to operate a LRCS measurement range.

Format of the Measurement Range

A schematic of the range is depicted in Fig. 2.1 and Fig. 2.2. A
pulsed Nd:YAG laser operating at a wavelength of $1.064 \mu m$ is the source
of the emitted optical wavefront. This wavefront first passes through a
negative lens, for reasons that will soon be explained. The wavefront
next strikes a microscope slide, which is being used as a beamsplitter.
This microscope slide partially reflects, towards the first of two
detectors, a small portion of the energy contained in the incident
wavefront. This detector, in turn, responds by emitting a representa-
tive electrical signal which is used as a reference trigger for the data
collection equipment. Most of the original wavefront continues to
propagate beyond the microscope slide and then, in the laser's far field
(7.3 meters from the reference point), overfills the target. Depending
on the target's size, shape, orientation, and backscatter characteris-
tics at $1.064 \mu m$, some part of the incident wavefront scatters back
towards the source. It is the sensing of this return optical energy
which constitutes "detection of the target." The amplitude of the

8

TARGET
PLANE

731.5 cm
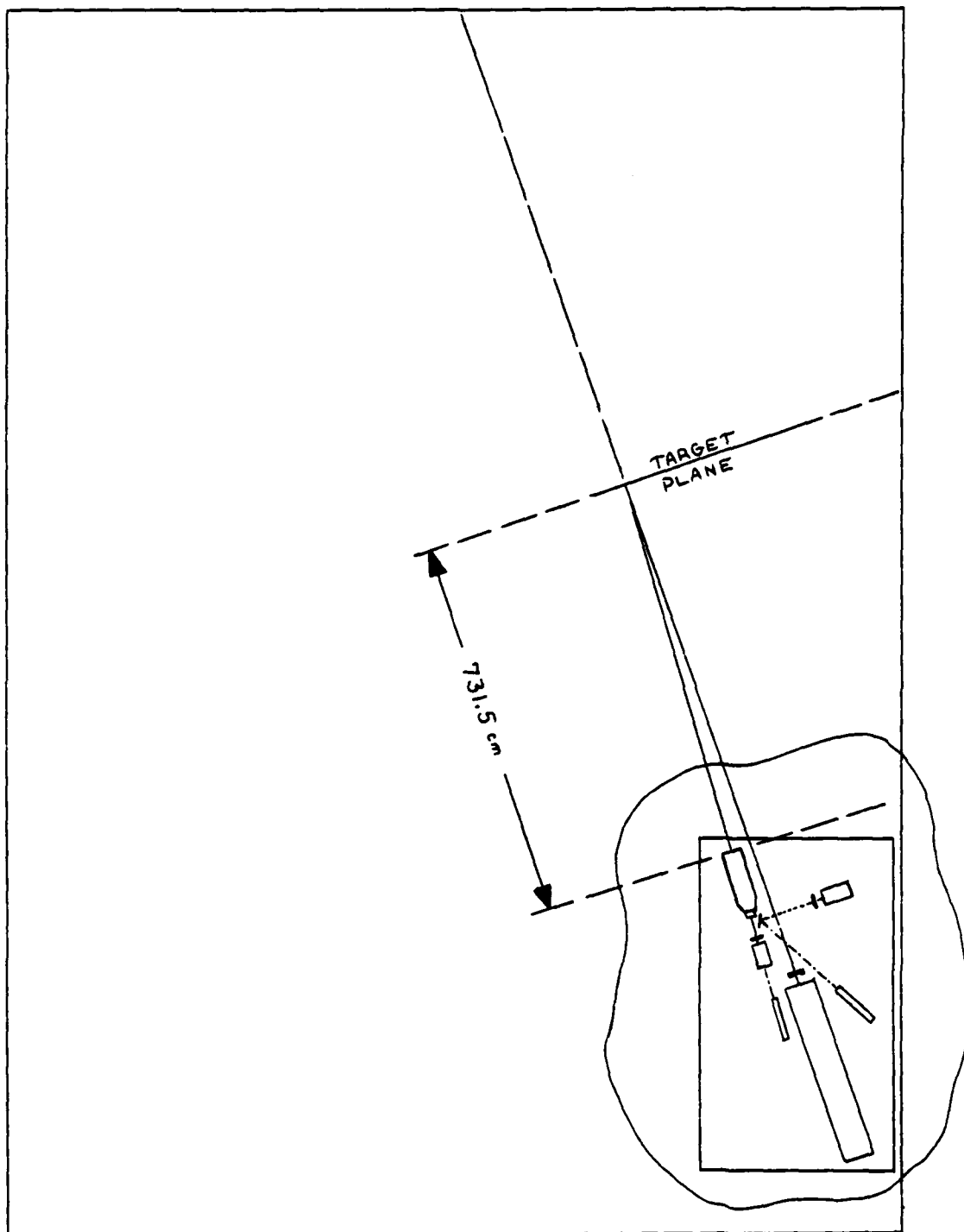
Fig. 2.1. LRCS Measurement Range (Plan View)

9
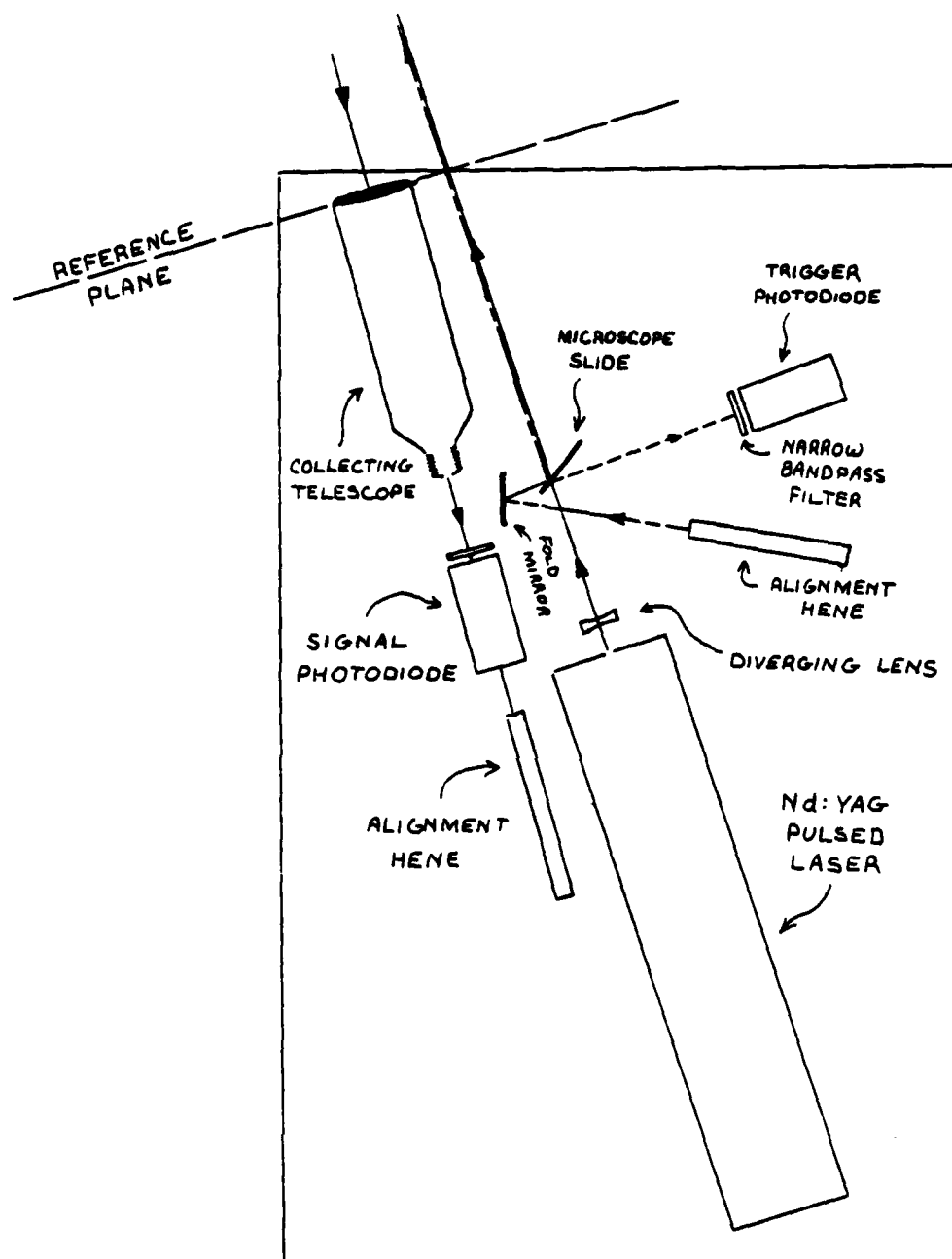
Fig. 2.2.   The Emitter-Receiver Set-Up

(Enlargement of Region Encircled in Fig. 2.1)

10

return signal is linearly related to the LRCS of the target. In order to enhance the sensitivity of these measurements, intermediate optics are used to capture a larger portion of the backscattered signal and then converge this signal so that it just fills the smaller active region of a second detector. Under ideal conditions, the entire target should be imaged by the intermediate collecting optics onto most of this detector's active area. This approach would guarantee that the signal-to-noise ratio (SNR) is maximized within the limitations imposed by the target's geometry. The electrical signal generated by this second detector is displayed either on the CRT screen of a very fast storage oscilloscope, or when more detailed analysis is required, on the display of a complev signal processor which has been integrated with a boxcar averager.

In this experiment, the line of sight of the laser illuminator is not the same as the line of sight of the detector's collecting optics. This non-coaxial configuration is commonly referred to as a "bistatic" system. Although the data generated by this arrangement is much more sensitive to alignment errors in the target's position, it benefits from a higher SNR than could be achieved in a coaxial configuration, all other factors being equal. A coaxial configuration, in which both the EM wave transmitter and receiver have the same field of view, is common-ly referred to as a "monostatic" system.

Two independent Helium-Neon (HeNe) lasers are simultaneously used to ensure that each target is placed in the one spatial position that is exactly centered within the field's-of-view of both the laser and the return signal's collecting optics. One laser is co-aligned to the Nd:YAG laser's line of sight, while the other HeNe laser is co-aligned

11

with the optic axis which passes directly through the collecting optics.
It is where these two reference beams superimpose on one another that
the target's surface must be located.

Characteristics of the Nd:YAG Laser

One of the factors which most affects the intensity distribution of
the return signal is the target. Equally important, though, is the
intensity distribution of the incident signal (which is then scattered
in a unique way by the target). For this reason, that incident signal
should be well characterized. Under ideal conditions, the incident
wavefronts would be planar with a uniform constant amplitude across
their surfaces. Every effort has therefore been made to approximate
this ideal condition.

The Nd:YAG laser chosen for this project was an International Laser
System's (ILS) model LL-102-20. It was selected because of its rather
short pulsewidth, a nominal 30 nsec full-width-at-half-maximum (FWHM).
This size pulsewidth is short enough in duration to allow temporal
distinction between a return signal from a target and that from back-
ground clutter located only 5 meters beyond the target. (5 meters
separation equates to 10 meters round trip optical path length; at the
speed of light, this distance is traveled in approximately

$$\frac{10 \text{ METERS}}{3 \times 10^{8} \text{ METERS/S}} = 33.\overline{33} \text{ nsec} \tag{5}$$

which is a peak-to-peak separation that certainly satisfies the Rayleigh
criteria for resolution of two consecutive pulses.) Had the pulse width
been much shorter in duration, its size would have approached the "read"

rate of the data collection equipment. The error bars associated with those measurements would have been unacceptable.

An optical schematic of the laser is presented in Fig. 2.3. The resonator optics consist of two porro prisms which are oriented 90° from one another about the cavity's optical axis. In other words, the roof edges of each prism are perpendicular to one another. The Nd:YAG laser rod measures 5 mm in diameter by 75 mm long and is optically pumped by a Xenon flashlamp. Q-Switching of the laser is performed by a Pockels Cell. A dielectric polarizer is sealed between two right angle prisms which are joined symmetrically to form a cube (see Fig. 2.3). In this "cube," the right angle prism closest to the YAG rod is responsible for partially coupling out the laser pulse from the cavity. Two additional lenses found within the resonator expand the beam and compensate for positive focusing that occurs within the laser rod. An adjustable iris also exists within the cavity for control of higher order modes (ILS Operation, Maintenance, and Service Manual, 1979:2-10).

During the experimental build-up, the iris was slowly closed until the output beam appeared to have a gaussian irradiance distribution (as viewed on photosensitive paper). At this point, the diameter of the iris was 2.955 ± .003 mm and the energy in each pulse was certainly less than the .1 joules (J) expected with the iris completely open. The average of 10 measurements, listed in Table 2.1, indicate that the average pulse energy is in fact .0166 ± .0003 J. Since the limiting aperture in the cavity is the iris, it is reasonable to initially assume that the spot size at this point is the waist, w_o, of the laser. If the two compensating lenses were not also within the cavity, the calculation of the Rayleigh range could be done accurately:

13
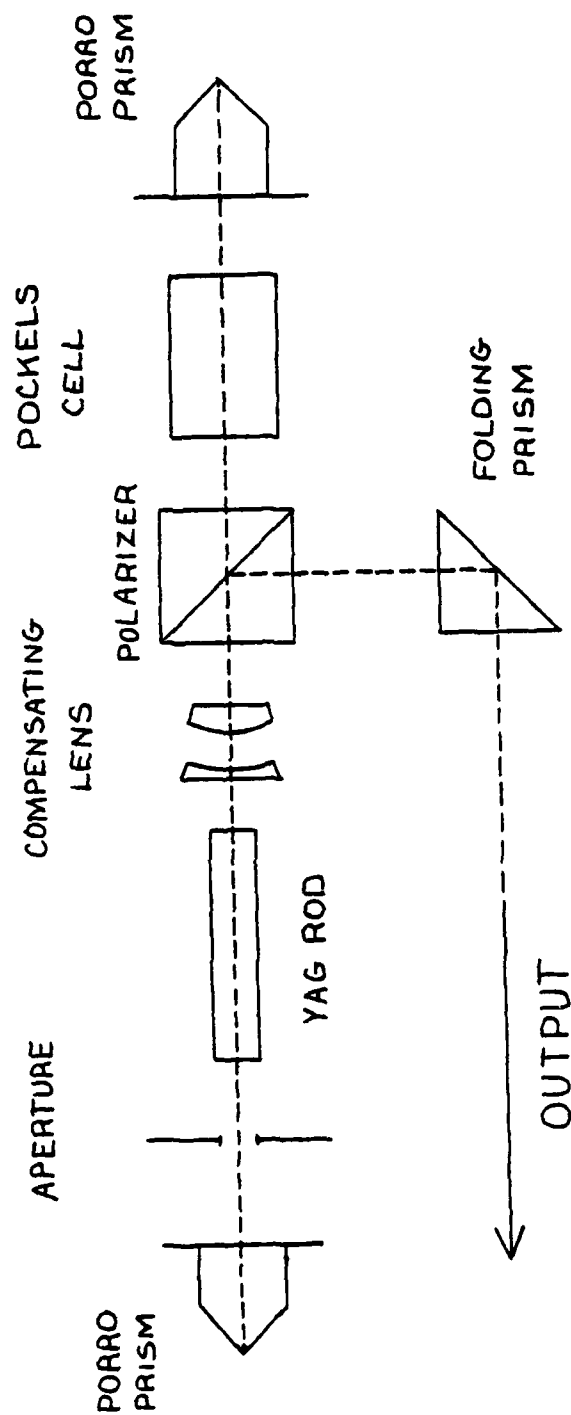
Fig. 2.3. Optical Schematic of the Nd:YAG Laser

1 - .0167 J	6 - .0161 J
2 - .0163 J	7 - .0169 J
3 - .0164 J	8 - .0163 J
4 - .0170 J	9 - .0167 J
5 - .0168 J	10 - .0169 J

MEAN VALUE	= .0166 J
MEDIAN VALUE	= .0167 J
STANDARD DEVIATION	= .0003 J

Table 2.1. Measurements of Pulse Energy

$$\text{RAYLEIGH RANGE} \ = \ \frac{\pi \, w_0^2}{\lambda} \tag{6a}$$

$$Z_R \ = \ \frac{\pi \, (1.477 \text{ mm})^2}{(1.064 \times 10^{-3} \text{ mm})} \tag{6b}$$

$$Z_R \ = \ 6.44 \ \text{METERS} \tag{7}$$

Because of the effects of the compensating lenses, the Rayleigh Range is actually larger. This means that at a range of 6.44 meters from the location of the waist, a target would not yet be located within this laser's far field. The spot size at the laser's output is 1.58 ± .02 mm. Since it is reasonable to presume that this value is larger than

15

the effective waist of the cavity, a sufficient upper limit for z_R can now be computed. Using Eq (6a), the Rayleigh Range is found to be less than 7.37 meters. The importance of this is that, in the far field, the rate of divergence of the laser wavefront is constant. Measurements of the two spot sizes in the far field indicate a far field half angle of 4.48 milliradians. Since all of the targets will be measured at a range of 7.3 meters, careful measurements of the irradiance distribution of a pulse were made at this range. This data was gathered by slowly translating a photodiode detector (masked by either a .20 mm or a .50 mm slit) along a path perpendicular to and intersecting the Nd:YAG laser's optical axis. A number of measurements of local irradiance were made for each detector location and for each of the two slits. The plots of the average pulse irradiance profile are depicted in Figs. 2.4 and 2.5, and error bars are provided for each measurement made. Although the large size of the error bars associated with the most intense central points prohibit precise identification, the expected gaussian transverse-amplitude variation across the pulse's wavefront fits the profile. As a consequence of the Q-switching method employed, the laser light is also linearly polarized with its electric field vector aligned along the horizontal axis.

The Diverging Lens

The target's return signal can be best interpreted if there is some margin of consistency across the wavefront which first strikes the target. Although the ideal condition (i.e., a perfectly plane wave with a uniform constant irradiance) can never be realized, a very good ap-proximation of this can be achieved with the proper choice of a negative
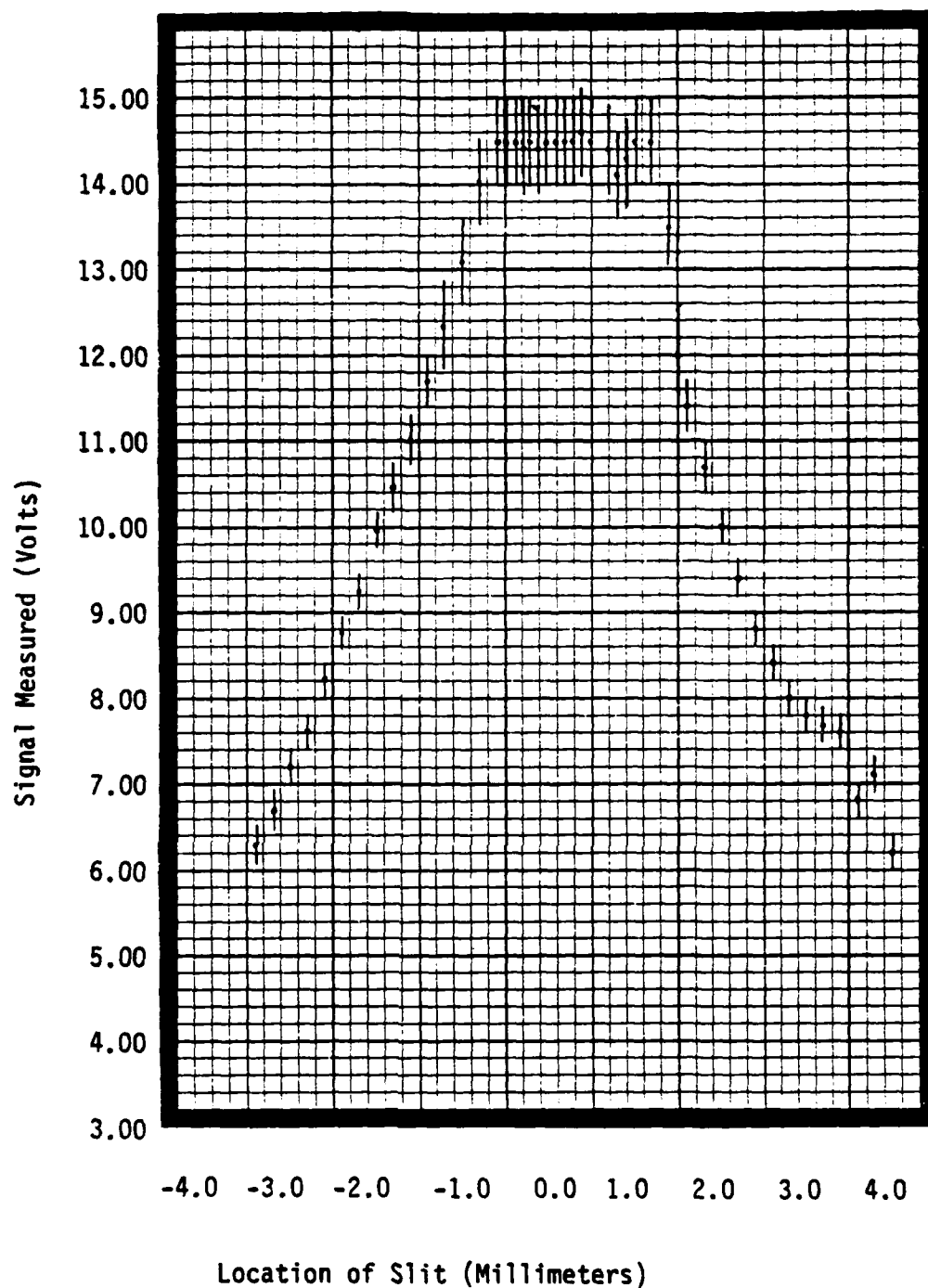
Fig. 2.4. Nd:YAG Pulse Spatial Irradiance Profile (.50 mm slit)

(Amplitude Attenuated by 4.00 N.D. Filter)

17
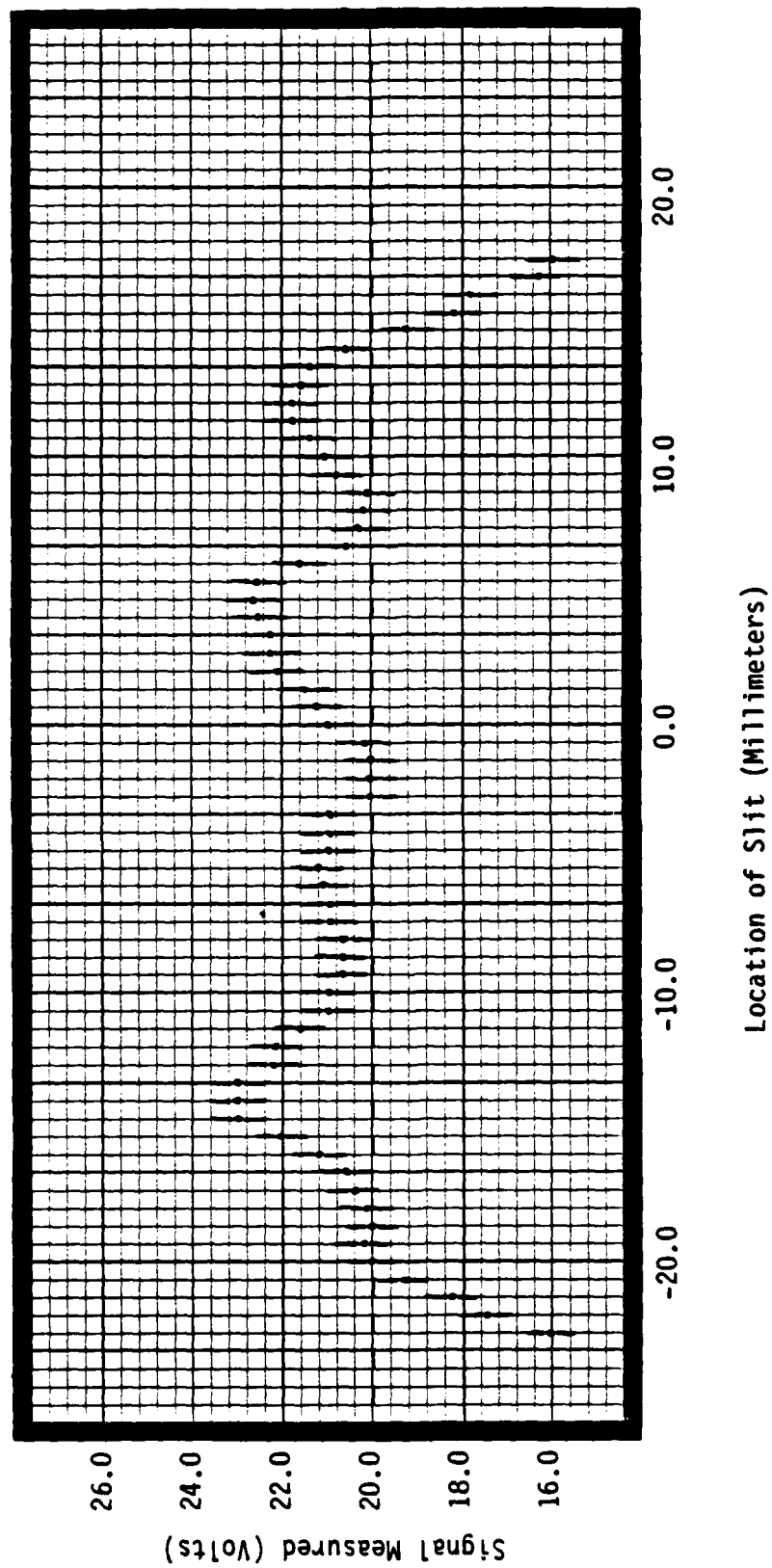
Fig. 2.5. Nd:YAG Pulse Spatial Irradiance Profile (.20 mm slit)(-600 mm F.L.
Diverging Lens Installed at Laser Output)

18

lens at the laser device's output. Because a gaussian spherical
wave is essentially emitted by the laser, the pulse's most central
region is much like a plane wavefront of constant irradiance.
Unfortunately, the region within which this is true is also very
small. By diverging the emitted beam, this acceptable central
region can completely overfill the target. The only penalty paid
is a reduction in the amount of optical energy available to be
scattered. A judicious choice of a bi-concave, -600 mm focal
length lens resulted in an acceptable central region of diameter
3.55 cm at the designated 7.3 meter range.

Spheres as Calibration Standards

A single definition of a LRCS has not been universally accepted
throughout the scientific community. This is consistent with the
disagreement over the form of the laser radar range equation. A cross-
section, at any frequency (whether microwave or optical), is a conve-
nient parameter for characterizing a target. It should be described by
a single numerical value which is a function of the static properties
(i.e., size, shape, composition, etc.) and, if applicable, the dynamic
properties of the target (Bachman, 1979:52-56). This single numerical
value directly relates the LRCS for the unknown target to that for a
very well characterized standard. Herein lies the disagreement concern-
ing the LRCS definition. Two different calibration standards exist for
LRCS measurements, and each has served a purpose by describing the size
of the return signal to be expected from targets of similar composition.
The first standard, a theoretically lossless diffuse flat plate, is the
most commonly used (Wyman, 1968:1). For this reference, the LRCS of a

19

target is defined as "the area of a non-absorbing, planar, perfectly lambertian surface which, when substituted for the target and oriented perpendicular to the ladar line-of-sight, produces a scattered irradiance at the receiver equal to that of the target. (Common experimental approximations to the diffuse standard include such surfaces as magnesium oxide and flame-sprayed aluminum)" (Bachman, 1979:184). The second standard sometimes used is an "isotropic specular sphere; that is the target's LRCS can be considered to be the equivalent cross-sectional area of a perfectly reflecting specular sphere which produces a reflected intensity at the receiver equal to that of the unknown target. It can be shown that the intensity from a spherical reflecting surface is given by

$$I(z) = \frac{I_1 R^2}{4 z_1^2} = \frac{I_1 A_{cs}}{4 \pi z_1^2} \qquad (8)$$

where

I_r = reflected intensity
I_1 = incident intensity
R = radius of the spherical surface
Z_1 = the range from the spherical surface
A_{cs} = the spherical surface's cross-sectional area"

(Bachman, 1962:183-184).

Two different calibration standards are not necessary. Only one is ever required, and its two utmost criteria need only be its consistency and availability. It is the spherical standard which, although more difficult to preserve as a high reflector, has become the highlight of this experiment. This is in terms of both its use as a reference target for other LRCS measurements and as a theoretical scattering problem to be examined and better understood. This latter investigation is, in

20

fact, the entire subject of Chapter III.

Very high grade steel ball bearings of 13 different sizes have been selected to represent the highly reflecting spheres in the experiment. Although there is little information on their nominal reflectivity at 1.064μm, it can be assumed to be greater than 95%. Produced by Hoover Universal Inc. of Cumming, GA., they are of grade "5" with a deviation from sphericity of no more than 5 x 10^{-6} inches (Hoover Universal, 1983). The diameters of the test spheres, measured in inches, are: 1 1/4, 1 1/16, 15/16, 3/4, 11/16, 5/8, 1/2, 7/16, 3/8, 5/16, 1/4, 3/16, and 1/8.

Collecting Optics

Some targets will have a very small LRCS at λ = 1.064μm. It was therefore determined that the detector available might not be sufficiently responsive. Four alternatives existed:

1) a photomultiplier tube (PMT) with inherently high gain could be used instead of the fast photodiode selected,

2) the range could be reduced,

3) the energy in the incident laser pulse could be increased or,

4) more of the return signal could be captured and then concentrated on the photodiode.

A PMT would have been awkward to align and more cumbersome to use. Shortening the range would have moved the target's location into the laser's near field. Upgrading the laser's pulse energy would have been unnecessarily time consuming. Only in the last choice was there both simplicity and a second benefit. By using a variable focus telescope (see Fig. 2.6) to collect a bigger portion of the backscatter signal,

ONE NEGATIVE
LENS WITH
ADJUSTABLE
POSITIONING

THREE FIXED OPTICAL
ELEMENTS SEPERATED
WITH AIR GAPS
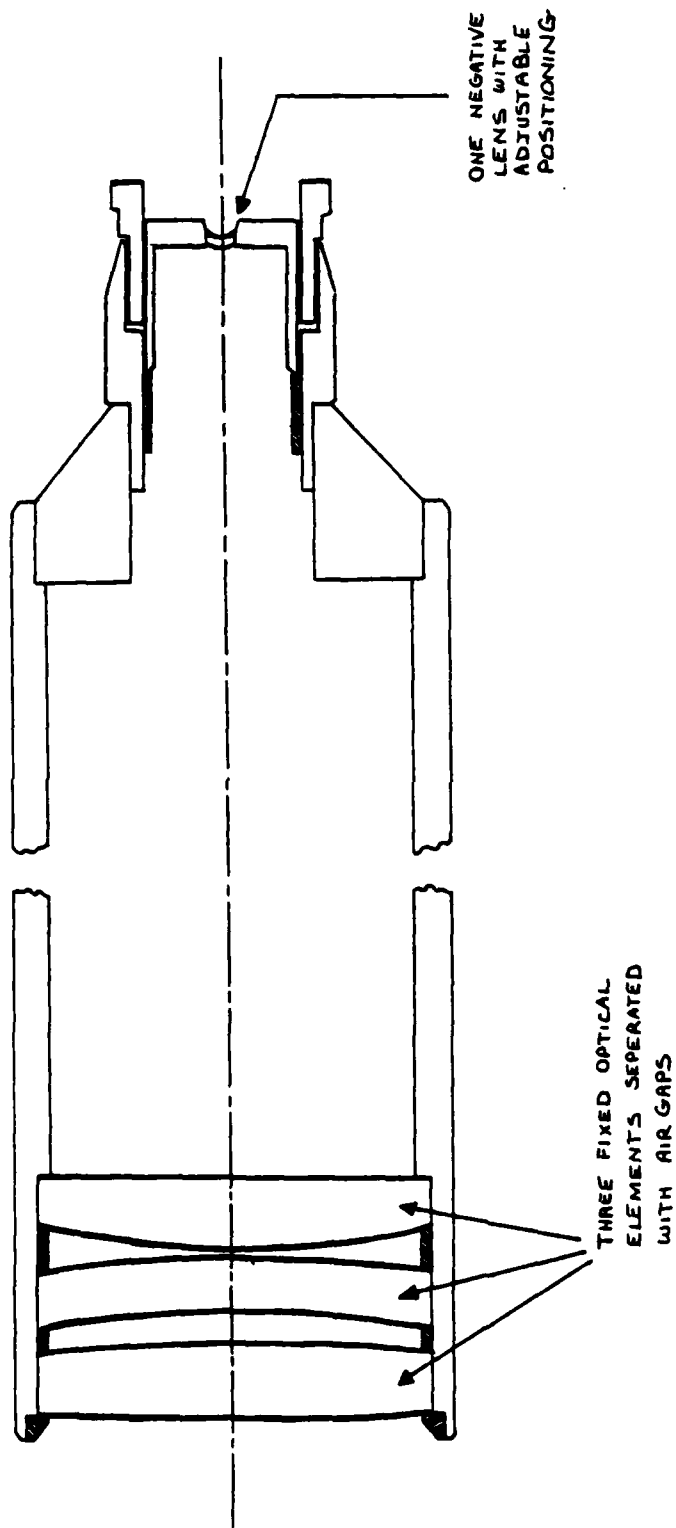
Fig. 2.6. Schematic of Collecting Telescope

(no additional technical information is available)

22

the photodiode's field of view could also be controlled. By imaging the entire target (and as little else as possible) onto the active region of the detector, the chances were minimized that stray energy from other reflections would feed back into the photodiode. Built by Special Optics Inc., the telescope contains four refracting elements and was designed for high transmissivity at $1.064 \mu m$ with only $\lambda/10$ wavefront distortion.

Signal Detection

The LRCS measurement range required two detectors: one to trigger the signal recording equipment, and a second to actually measure the return signal. The device selected for both applications was an ultra-fast silicon photodiode called the FND-100. Produced by EG&G, it rivals a PMT in performance except that it does not provide low noise signal gain. Its characteristics are listed in Table 2.2 and its spectral response is plotted in Fig. 2.7. It has a circular active area of 5.06 mm² (smaller in size than the 19.63 mm² exit lens of the collecting telescope) and is a unit compact enough to be physically translated by a micrometer in two dimensions. The spectral response curve indicates that approximately .253 ± .005 amps/watt can be expected from the FND-100 at $\lambda = 1.064 \mu m$ but care must be used to ensure that the return signal does not overfill the active area on the photodiode's front face. The details of the alignment that guarantees this condition are presented in Chapter IV. Uniform neutral density filters were employed to ensure that each photodetector would be performing well within its linear operating region.

Active area	$= 5.1$ mm^2
Wavelength	$= 300-1100$ nm
Bandwith	$= 350$ MH
Responsivity	$= 0.62$ A/W @ 900nm
Rise time (10-90%)	$= 1$ nsec @ 50
Breakdown Voltage	$= 125$ V
Capacitance	$= 8.5 \times 10^{-12}$ F
Series Resistance	$= 35$ ohms
Dark Current	$= 100$ namps
Noise Current	$= 1.8 \times 10^{-13}$ amp/Hz$^{1/2}$ @ 1 KHz
NEP	$= 2.9 \times 10^{-13}$ W/Hz$^{1/2}$
Operating Temperature	$= -55$ to $+70°$ C
Linearity	$= \pm 2\%$ over 7 decades

Table 2.2. Typical Performance Characteristics of the FND-100

With a 90 Volt Bias (EG&G Data Sheet D3013b-1)

Signal Storage and Processing

When optical energy strikes the active region of the FND-100, a representative electrical signal is generated with a rise time of 2-3 nsecs. This signal travels through 2 meters of RG-58 coaxial cable to the data storage instrument which has an input impedance of 50 Ω . Provided that the instrument has been properly triggered to begin writing a time-history of the electrical voltage that it receives, the CRT screen will display the pulse. Herein lies a common difficulty with

24
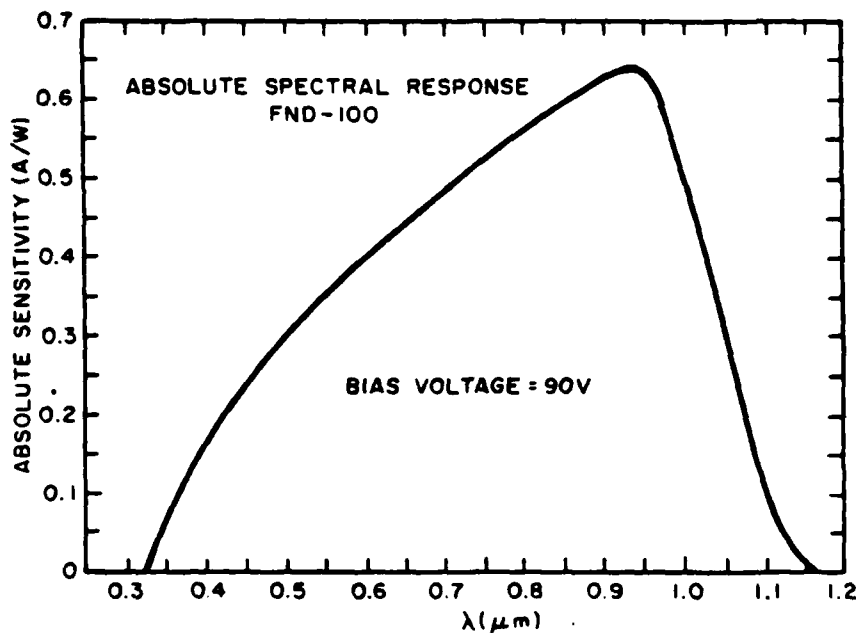
Fig. 2.7. FND-100 Absolute Spectral Response

(EG&G Data Sheet D30138-1)

measurements of very short laser pulses. Non-laser optical energy is generated by the flashlamp long before the laser pulse is created. This non-laser energy is first detected and can trigger the writing function of the data storage equipment; these events unfortunately occur much too soon for any useful laser pulse information to be recorded. The solution to this dilemma involves the use of narrow bandpass filters, each with a maximum transmittance at $\lambda = 1.064 \mu m$ and a bandwidth of only 52 Å. These filters, positioned across the entrance to the photodiodes, seal out all spurious non-$1.064 \mu m$ light. Although flashlamp emissions exist at $1.064 \mu m$, the intensity is purposefully below the trigger's thresh-

25

old.

The first of two types of storage equipment used are a Tektronix Storage Oscilloscope (Model #7834) with two plug-in modules: a Dual Trace Amplifier (Model #7A26) and a Dual Time Base (Model #7B53A). This unit provides a quick and accurate record of a single pulse's temporal profile. As such, it is the workhorse for all alignments and quick measurements. The second data storage system used is an EG&G Model 4400 signal processing system, composed of a Boxcar Averager (#4420), a Gated Integrator (#4422) and the actual signal processor (#4402). The system, although much more time consuming to use, is capable of performing an indepth analysis of the scattered energy which is measured by the second FND-100. Its CRT display is identical to that of the oscilloscope's in format. The 4400 system's display, however, is not a continuous function, but rather is broken up into a series of discrete points. Each point represents the average value of the signal measured across a small interval of the pulse, The penalty for this type of operation is paid in terms of time and laser stability. Many pulses are required (one for each discrete point) in order to profile an "average" pulse. This averaging operation is only useful when laser stability has been achieved. Nonetheless, the 4400's supporting software provides post-data acquisition processing which is unavailable on an oscilloscope.

Background Reflections

Almost every material reflects some energy at $\lambda = 1.064 \mu m$. Although this is generally a desired feature in a ladar system, it can also be a source of errors if calibrated measurements are to be made.

It is therefore of the utmost importance to identify and control the undesired reflections which can feed back onto the signal detector. "Even very small ladar signals can become detectable by filtering out as much optical background clutter, or noise, as pos ible. The filtering can be spatial, temporal, or spectral" (Bachman, 1979:88), but this ladar measurement range uses a combination of all three of these methods.

Spatial filtering was employed through the use of the collecting telescope which, by its very nature, significantly reduced the signal detector's field of view from its original 2π steradians. By selecting a field of view that just included the target, the influence of many significant sources of unwanted backscatter was eliminated. Some inescapable sources of clutter were still within this limited field of view; these included the rear wall of the laboratory and the support structure for the targets.

The location of the wall could not be changed, and surprisingly enough, its return could only be marginally reduced by shrouding the wall with other absorbing materials. Bachman, in a short commentary on LRCS measurement ranges, suggested hiding the effect of the wall with "an ordinary glass aquarium tank oriented at a skew aspect angle to the incident pulse and filled with water darkened by black ink." A better solution was found by the judicious use of temporal filtering. By moving the target in from the rear of the room so that it was now a good distance from the back wall (but still located in the laser's far field), the return from the wall was now distinguishable in time and separable from that of the target. By further orienting the experiment so that the incident and return line of sights were approximately 17°

27

from the wall's normal, the irradiance of that backscattered return was significantly reduced.

Spatial and temporal filtering were of little use in dealing with the return caused by the target's support structure. The use of cotton string to hold the spherical targets was desirable because of the string's almost negligible LRCS, but the ball bearings chosen as spherical standards required precise alignment. This could not be achieved and maintained using cotton string. Because of the hardness of the ball bearings, machining any portion of their non-irrradiated hemisphere caused damage to their opposite surface. Because of the importance of high surface quality in this calibration, this operation was not considered, and non-vertical rigid support of the spheres was decided to be impractical. Although not ideal, the final choice for support structures were 6 cylindrical lucite rods with highly buffed surfaces. Only one rod, of smallest possible diameter and with one end spherically lapped to match a specific ball, was required for support. Each ball bearing of different size was assigned to the smallest lucite rod which would support it. These rods had a reflecitvity at $1.064 \mu m$ of approximately 7.5% (U.S. Precision Lens, Inc., 1973:17), and the small portion of the incident pulse which was actually reflected back into the capturing telescope was very small. Multiple reflections, although possible, were not considered probable. The most convincing argument is, by far, made by comparing the return from a supported sphere and that from just the rod (when the sphere has been removed). The return from the rod alone is, on overage, only responsible for 15% of the net measured signal.

The temporal profile of the return signal should consist of two

consecutively positioned peaks, the first from the target and of much

greater magnitude than the second, which is due to the wall. With the

careful location of a vertical aluminum rod near, but not in, the main

beam path, a third small peak can be introduced to the profile. It

precedes the others mentioned and represents a reference for the outgo-

ing wavefront-as it leaves the experimental table (see Fig. 2.8). The

final temporal profile is then composed of three peaks, all with the

same generic shape but with vastly different profiles (see Fig. 2.9).

The first and last of the three pulses provide convenient reference

marks throughout the measurement process for the location of the expect-

ed LRCS returns.

REFERENCE
POST

WAVY LINE REPRESENTS THE
CLEAR LINE OF SIGHT BETWEEN
THE REFERENCE POST AND THE
SIGNAL DETECTOR
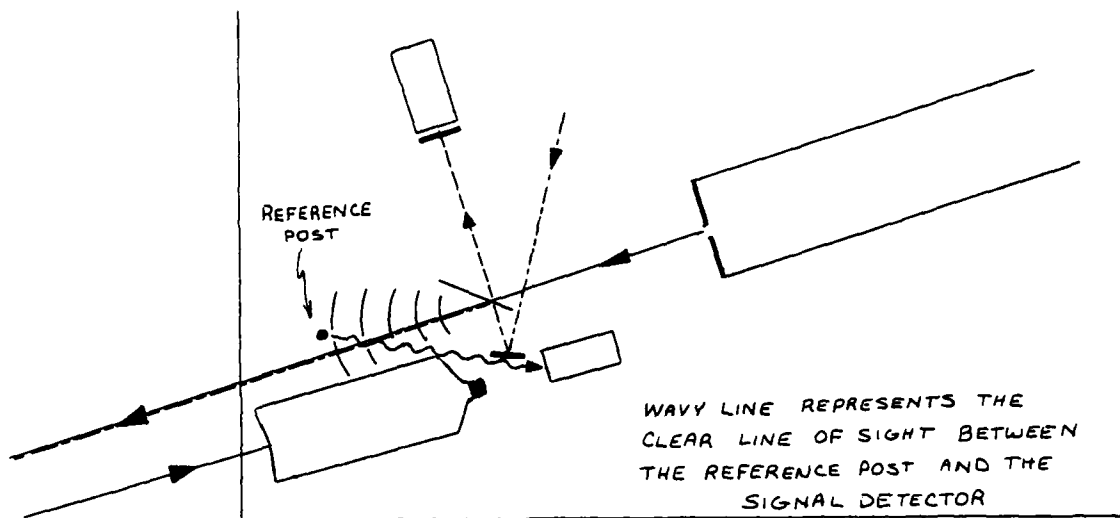
Fig. 2.8. Schematic of Experimental Table Identifying
Reference Signal Feedback Mechanism
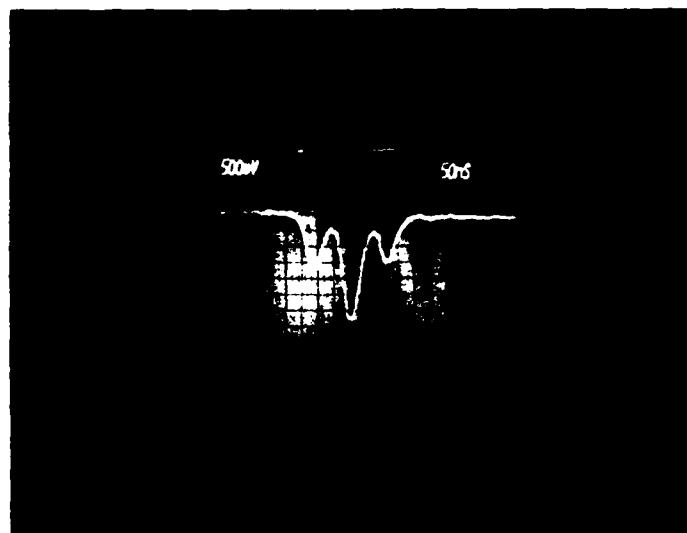
Fig. 2.9. Generic Termporal Profile of the Reference Peak
(on the left), the Target's LRCS Return (in the center),
and the Signal Reflected by the Back Wall in the Laboratory
(on the right)

30

III. Laser Pulse Scattering Theory

An Overview of the Analytic Developments

In order for a highly reflecting sphere to be used as a standard against which other LRCS measurements are made, its own LRCS must first be defined. Historically, this type of requirement has repeatedly generated the same controversy: against what should the "standard" itself be standardized?

The general approach to avoid this dilemma has typically involved simplifying the problem, by identifying the specific relationship that exists between the standard and the magnitude of its return signal. This relationship blindly accomodates all of the experimental constants which, if varied, would affect each measurement. Accounting for each of the experimental constants would be the first step towards calculating the absolute size of the return signal expected at the detector. The list of experimental constants is quite large, and includes the ladar beam's degree of coherence, its profile, wavefront curvature, and size relative to the target. It can include polarization (if the detector is polarization sensitive), and atmospheric distortion and absorption. In fact, the list contains so many different parameters that complete theoretical characterization of a target may not be possible. It is for this reason that the historical approach has been to universally define the LRCS of a perfect specular sphere to be, in the far field, the geometric projected area

$$\sigma_L \ (SPHERE) \ = \ \pi a^2 \ . \tag{9}$$

where "a" is the sphere's radius. This definition is independent of both polarization and bistatic angle (Danielson, 1977:17).

Despite the complexity involved, every attempt should be made to predict the size of the return signal expected when a sphere is the target. Correct analytical expressions for this return signal amplitude provide a basis for further theoretical analysis of some more complex targets. A mathematical approach to the problem of backscattering from a sphere is developed in this chapter. Using the techniques of geometric optics, it is a very good approximation because the sphere's smallest dimension is so much greater than the wavelength of the incident light. A superior approach uses physical (or wave) optics in a more precise treatment of the problem. This derivation is performed in detail in Appendix C, but final numeric predictions are not made. The exact solution of the wave equation for scattering of a plane, linearly polarized monochromatic wave by any homogenous sphere of arbitrary size was derived by Gustav Mie in 1908 (Asano and Yamamoto, 1975:29). Although it is a classical work, seemingly of great significance to this effort, Mie scattering theory will not be applied to this specific problem. His theoretical solution is expressed, in series form, in terms of Legendre polynomials and spherical Bessel functions (Stratton, 1948:VI). For particles of the same order size as the incident wavelength, only the first few lower order terms of the series are of appreciable magnitude. As the ratio $\alpha = 2\pi a/\lambda$ increases (where "a" is the sphere's radius and "λ" is the spectral wavelength), many additional terms assume importance. "The evaluation of the Mie formula when only a few terms are considered is computationally tedious and very time consuming. To date, tables of light scattering functions have been

compiled for values of α only up to 200. For $\alpha = 5000$, the calcu-
lation is a formidable task for even a so-called super computer"
(Erteza, 1981:1005). The smallest sphere being examined in this experi-
ment has a radius of curvature of approximately .16 cm. For this
sphere,

$$\alpha = \frac{2\pi \ (.16 \ cm)}{1.06 \times 10^{-4} \ cm} \approx 9484 \tag{10}$$

Many of the larger spheres have an α greater than 100,000. For this
reason, the use of Mie's computations was not considered further.

A Model Founded on Geometric Optics

Geometric optics suggests that there is a one-to-one relationship
between every reflecting point on the sphere's surface and every point
within a community of points in the detection plane. The analytic
relationship which will now be derived using ray optics will relate
these two sets of corresponding points. Since the location of the
collecting telescope's entrance aperture in the detection plane is well
known, it is possible to determine the effective area on the sphere's
surface which re-radiates energy measured by the detector. If a plane
wave of constant amplitude illuminates the sphere, then the reflected
energy captured by the telescope should be

$$E_{EXPECTED} = \mu \ A_{eff} \ \Gamma \ \eta \tag{11}$$

where

μ = energy density of the incident wavefront

33

A_{eff} = surface area of the sphere, projected onto a plane, which re-radiates that energy collected by the telescope.

Γ = reflectivity of the sphere at 1.064

η = single pass attenuation of the laser energy by the atmosphere

It will be assumed that both μ and Γ are constant values for all points on the sphere. Fig. 3.1 depicts the scattering problem in two dimensions. The greatest off-axis observation point, r_{max}, is 22.4 cm. At a fixed range of 731.5 cm, the greatest angle, 2θ, between an incident ray and its reflection can be determined by examining a limiting case. If nothing but the sphere's size could be changed, then the largest scattering angle (2θ) would be measured for an infinitely small sphere. This is because ρ would also be a minimum value, approximating zero. For this example, the largest possible angle is

$$\tan 2\theta_{MAX} = \frac{22.4 \text{ cm}}{731.5 \text{ cm}} \tag{12a}$$

$$= .030622 \tag{12b}$$

$$2\theta_{MAX} = .030612 \tag{13}$$

The numeric solutions have been displayed to six decimal places in order to demonstrate the following point. For the very small values of θ expected in this problem, small angle approximations will be quite valid.

$$2\theta_{MAX} \approx \sin 2\theta_{MAX} = (.030608) \tag{14}$$

34
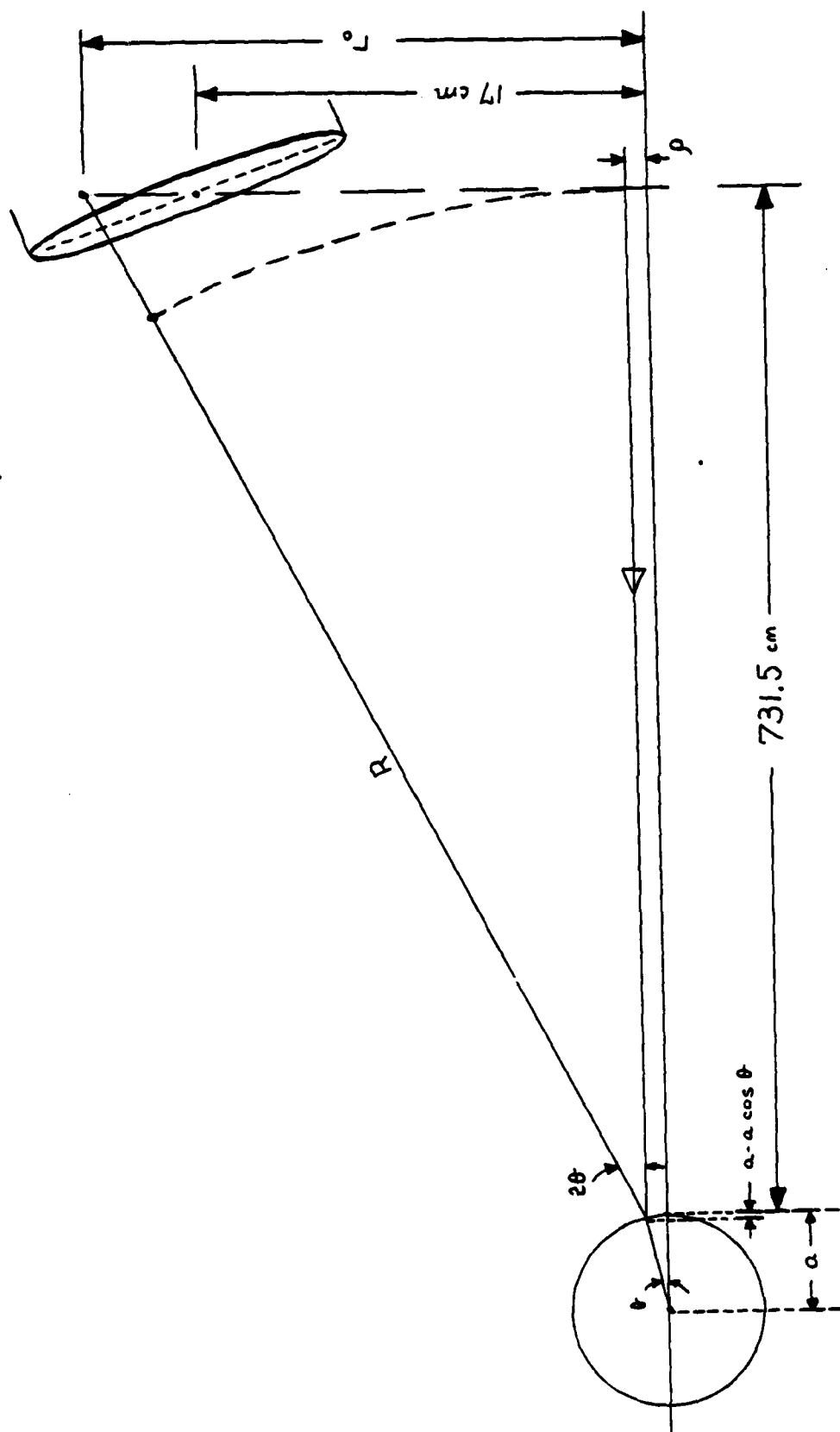
Fig. 3.1. Two Dimensional Analysis of the Scattering

Problem Within the Geometric Optics Limit

(not drawn to scale)

35

$$2\theta_{max} \approx \tan 2\theta_{max} = (.030622) \tag{15}$$

and

$$\cos 2\theta_{max} = .999531 \approx 1 \tag{16}$$

Using these approximations will generate a geometric error of no more than

$$\frac{(.030622) - (.030612)}{(.030622)} \times 100 = .03\,\% \tag{17}$$

The collecting telescope's entrance aperture does not lie completely in the plane represented by $z=z_i$ (see Fig. 3.1). If no approximations were allowed, the aperture would have to be mathematically described as lying centered and tangent to the circle of radius (z_i-a) and with center at $(0,0,a)$. Instead, because of the small angles and relatively long ranges involved, the aperture can be treated as if entirely with in the $z=z_i$ plane. Referring to Fig. 3.2, the error associated with this approximation is calculated below.

$$\tan 2\theta = \frac{x}{(z_i - a)\,\sin 2\theta} \tag{18}$$

therefore

36
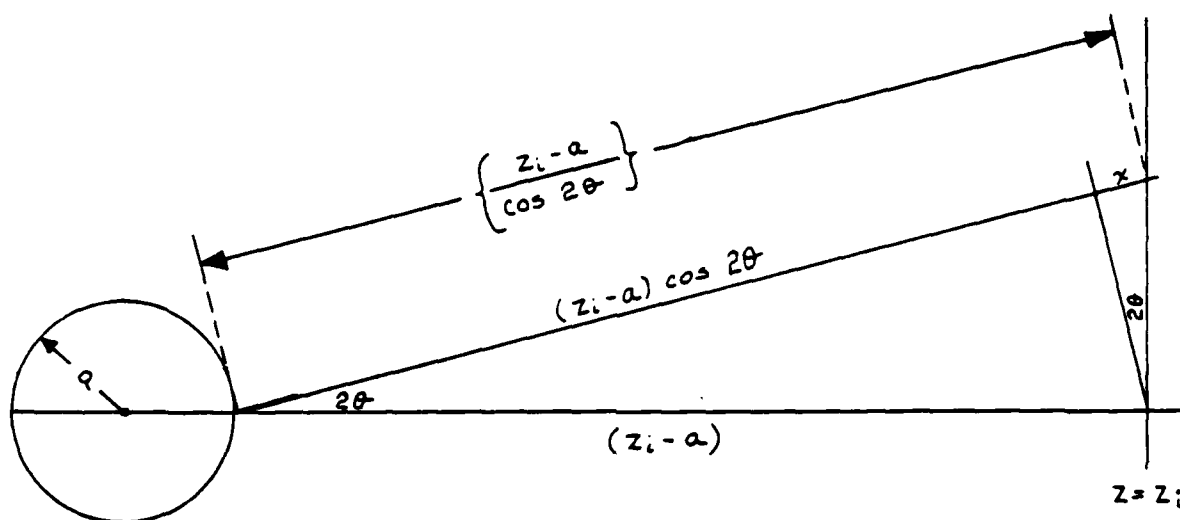
Fig. 3.2. Analysis of Telescope Alignment Error

$$x = (\tan 2\theta)(\sin 2\theta)(z_i - a) \tag{19a}$$

$$= \frac{\sin^2(2\theta)}{\cos(2\theta)}(z_i - a) \tag{19b}$$

The fractional error is

$$\frac{x}{[(z_i - a)/\cos 2\theta]} \times 100 = 100 \sin^2(2\theta) \tag{20}$$

Since $2\theta_{max}$ = .030612 rad, $\sin^2(2\theta_{max})$ = 9.036 x 10^{-4}, and the final
fractional error is

$$100\,(9.036 \times 10^{-4}) = .09\,\% \tag{21}$$

Now that the necessary approximations have been justified for this
short derivation, please refer back to Fig. 3.1. In order to evaluate r_o
for every value of ρ in this two dimensional problem, we will follow
an approach applied by Rome Air Development Center (Demma and Michels,
1971:19-20).

37

$$\sin \theta \approx \frac{\rho}{a} \qquad (22)$$

$$\tan 2\theta = \frac{r_\circ - \rho}{z_i - a \cos \theta} \qquad (23)$$

Applying the acceptable small angle approximations

$$\sin \theta \approx \theta \approx \frac{\rho}{a} \qquad (24)$$

$$\tan 2\theta \approx 2\theta \approx \frac{r_\circ - \rho}{z_i - a} \qquad (25)$$

Therefore

$$\frac{2\rho}{a} = \frac{r_\circ - \rho}{z_i - a} \qquad (26)$$

$$2\rho(z_i - a) + \rho a = r_\circ a \qquad (27)$$

$$\rho \left[2(z_i - a) + a \right] = r_\circ a \qquad (28a)$$

and

$$\boxed{\rho = \frac{a r_\circ}{2 z_i - a}} \qquad (28b)$$

38

Using this relationship, the effective reflecting area of the sphere must be determined. The effective area is not the same as the surface area that contributes to the measured signal. Instead the effective area is equal to the surface area projected onto the incident planar wavefront. It is this area, multiplied by the wavefront's energy density, which equals the maximum energy measured by the detector under ideal conditions [refer to Eq (11)].

The three dimensional problem is now depicted in Fig. 3.3. Fig. 3.1 is, in fact, a two dimensional slice of Fig. 3.3, describing the geometry only in the plane which includes the optic axis and, coincidentally, both the points $(\rho, \varnothing, z)$ and $(r_o, \varnothing, z_i)$. The points in the z_i-plane, bounded by the telescope's aperture, must now be mapped to the z=a plane (see Fig. 3.4). The perimeter of the sphere's effective area can be determined by directly comparing it with the telescope's aperture. Because the mapping occurs according to Eq (28b), it is linear. Within the limits of the small angle approximations made, the map of a circular aperture will therefore also yield an effective area bounded by a circle. If, however, r_o were of a size significant compared to ρ, then the relationship between the two terms would become quite non-linear, and the effective area would be more or less "egg-shaped." This is demonstrated by a heuristic argument in Appendix A. The size of the circular effective area can readily be determined by comparing the corresponding on axis boundary points. Because

$$c - b \; < \; r_o \; < \; c + b \qquad (29a)$$
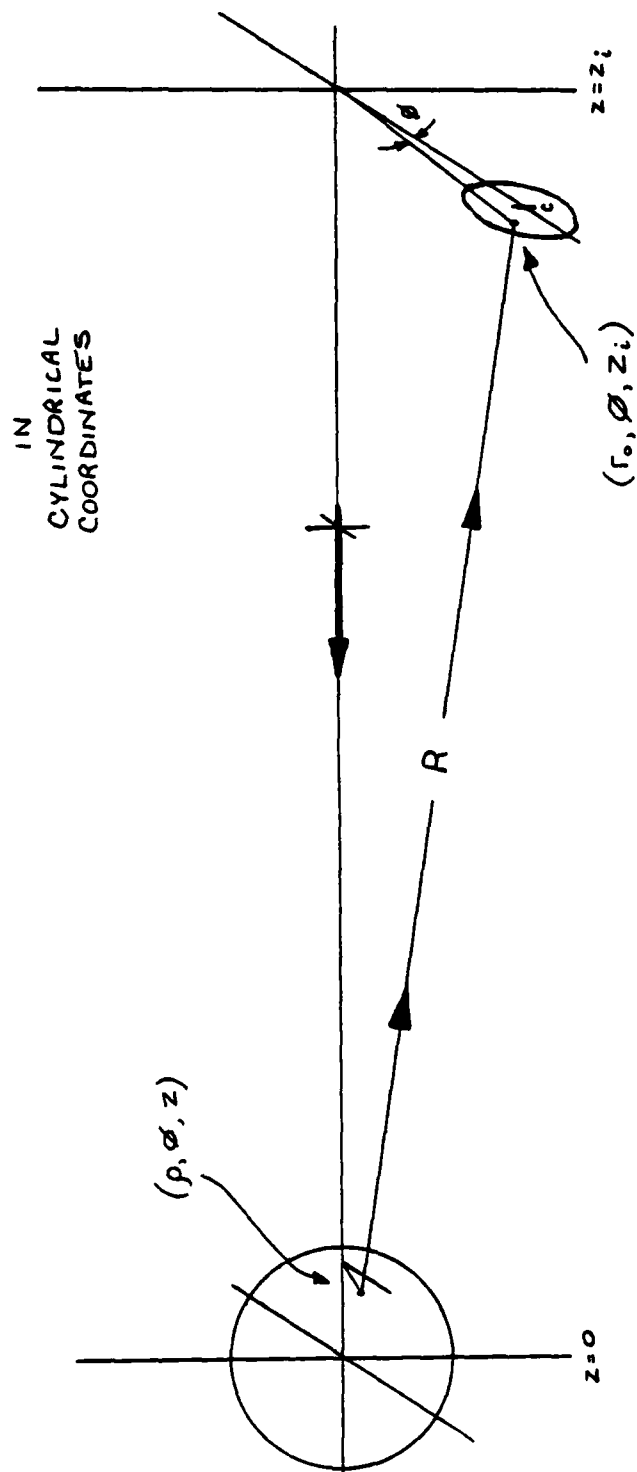
Fig. 3.3. Three Dimensional Analysis of the Geometric Scattering
Problem in a Bistatic System
(not drawn to scale)

40
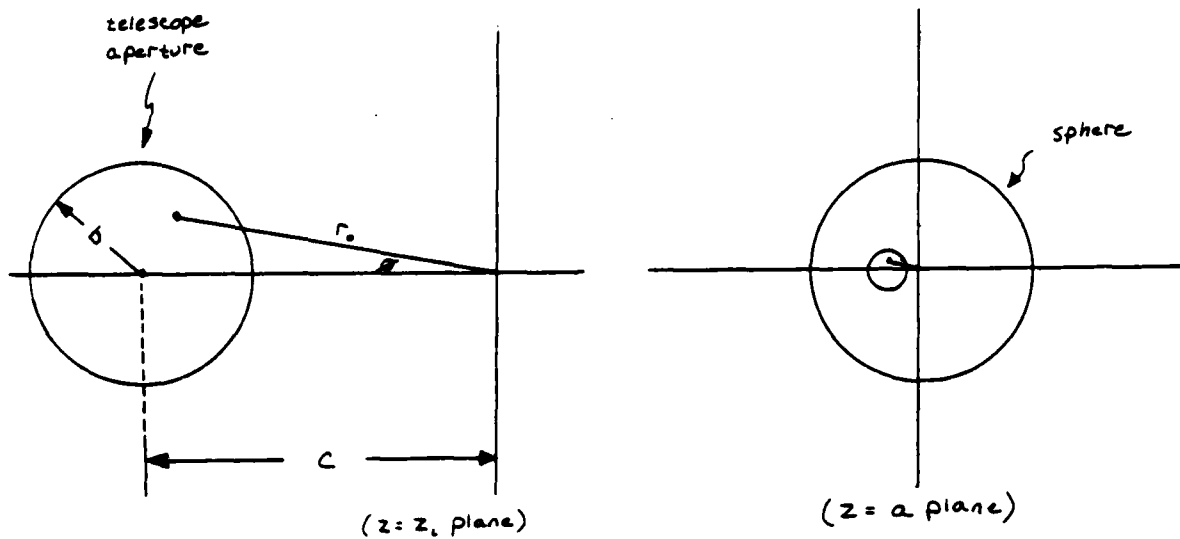
Fig. 3.4. Comparison of the Two Planes Between Which Mapping Occurs

(not drawn to scale)

$$11.6 \text{ cm} < r_0 < 22.4 \tag{29b}$$

$$\frac{11.6\, a}{2\,(731.5 + a) - a} < \rho < \frac{22.4\, a}{2\,(731.5 + a) - a} \tag{30}$$

For the largest sphere, $a = 1.587$ cm and

$$.013 \text{ cm} < \rho < .024 \text{ cm} \tag{31}$$

The effective reflecting area is therefore

$$\pi \left(\frac{.024 - .013}{2} \right)^2 = 1.0756 \times 10^{-4} \text{ cm}^2 \tag{32}$$

41

An estimate can now be made of the optical energy expected at the telescope's entrance. Measurements (see Fig. 2.5) indicate that the energy density at the sphere is on the order of 8×10^{-5} J/cm². Assuming that the reflectivity (Γ) is a constant 98% at 1.064μm, and that atmospheric absorption (η) in the laboratory contributes another loss of no more than 1%, then Eq (11) predicts

$$E_{EXPECTED} = \mu A_{eff} \Gamma \eta \tag{11}$$

$$= \left(8.17 \times 10^{-5} \; J/cm^2 \right) \left(.98 \right) \left(.99 \right)$$

$$\times \left(1.07 \times 10^{-4} \; cm^2 \right) \tag{33a}$$

$$= 8.485 \times 10^{-9} \; J \tag{33b}$$

If there were no absorptive losses during transmission through the telescope, and if the collected energy does not over fill the detector's active region, then the following electrical signal will be produced by the photodiode:

$$V'_{peak} = 50 \, \Omega \times (.253 \pm .005) \; A/\omega \times \frac{8.485 \times 10^{-9} \; J}{30 \times 10^{-9} \; sec} \tag{34a}$$

$$V'_{peak} = 3.578 \pm .070 \; V \tag{34b}$$

where

$$(.253 \pm .005) \ ^A/_\omega = \text{the calculated performance of the detector at}$$
$$\lambda = 1.064 \ \mu m$$

$$30 \ n \ sec = \text{the average pulse width (FWHM)}$$

$$50 \ \Omega = \text{the data equipment's effective input}$$
$$\text{resistance.}$$

However, no refracting telescope is perfectly transmissive. It is a good assumption that the losses are probably within 2%, so Geometric Theory predicts that the temporal profile of the laser pulse reflected off of the largest sphere will have a peak amplitude of

$$V'_{peak} \times .99 = V_{peak}$$

$$(3.578 \pm .070) \times .99 = 3.542 \pm .069 \ V \qquad (35)$$

Predictions of the returns from each of the 13 different sized spheres that will be measured are presented in Appendix B.

A More Rigorous Approach

The scattering of light from a sphere, as mentioned earlier, is really a diffraction problem. Wave optics therefore provides the pre-ferred approach to this problem's solution. In the geometric limit, it was acceptable to assume that the absolute intensity at a specific point in the telescope's aperture was due only to a reflection at a corre-spondingly unique point on the target sphere. This is only an ap-proximation of the solution specified in the realm of physical optics. The absolute intensity at any specific point in the aperture is, in fact, due to a linear superposition of all of the complex-valued field amplitudes. Each of these amplitudes is the result of contributions by

43

all of the points on the sphere's exposed surface, and each is weighted
by an obliquity factor as a function of location. This is just an
extension of the Huygen's Principle, which states that "every point on a
primary wavefront serves as the source of spherical secondary wavelets
such that the primary wavefront at some later time is the envelope of
these wavelets" (Hecht and Zajac, 1979:61). For the actual application
of this approach, refer to Appendix C.

IV. Experimental Procedures and Control of Errors

This experiment measures optical signals, emitted from a less than ideal laser source, which then scatter from the surface of an imperfect sphere. The energy is collected by an absorbing telescope and quantitatively measured by a detector whose output must then be amplified. Although these constraints seem to make it difficult to obtain accurate results, the errors are easy to contend with on an individual basis. The statistical variation in amplitude across the laser pulse's wavefront has already be presented in Fig. 2.5. The absorption in the telescope has been estimated to be approximately 2% at $1.064 \mu m$. The quality of the sphere, and the effects of amplification, will be discussed later.

The most difficult source of inaccuracies are those which result from mis-alignments. These errors are not as easily quantified and are, in fact, most easily addressed in terms of their net effect. This chapter will therefore present the techniques used to prepare and properly conduct the experiment. The alignment process will be reviewed, but not covered in minute detail; rather, attention will be given to unique problem areas and pitfalls to be avoided.

The Alignment Process

The bistatic nature of this measurement range (discussed on pg 11) complicates the process of collecting meaningful data. Each target sphere must be located in the unique spatial position that is exactly centered within the field's-of-view of both the laser and the collecting telescope. It is for this reason that the alignment of the telescope

45

and detector, and the alignment of the target, are inextricably linked. All of the following procedures can thus be fit into one of two categories:

1) those that are generic to all measurements, and

2) those that must be repeated for every new target.

Generic Procedures. The one constant in this experiment to which all other alignments will be referenced is the Nd:YAG laser's optic axis. This axis should intersect the diverging lens, the microscope slide, and the center of the target. With the lens removed, the microscope slide can be roughly adjusted to partially reflect the output laser pulse towards the trigger photodiode. Caution must be used because the output laser pulse is plane polarized along the horizontal axis. The nominal 45°-50° angle that the microscope slide makes with the Nd:YAG optic axis is very close to Brewster's angle. This angle (~57°) must be avoided if signal detection is to occur. For this reason, the microscope slide should be fixed at an angle that supports a strong reflection, and then, the photodiode should be positioned to intercept the reflected pulse.

The co-alignment of a HeNe beam with the Nd:YAG optic axis is the next goal. The HeNe laser that supports this will henceforth be referred to as "HL1." It can be translated from side to side and adjusted in both azimuth and elevation angles. This flexibility is used to position HL1's beam at the precise point on the back surface of the microscope slide which intercepts the Nd:YAG optic axis. This alone will not ensure co-alignment of the two beampaths. The fold mirror (FM-1) identified in Fig. 4.1 must then be adjusted to center HL1's beam

on the Nd:YAG optic axis in the far field. The HeNe spot on the micro-
scope slide will now be in error, so this alignment must again be
repeated. The two parallel techniques must be iterated until both are
simultaneously satisfied. It is then that the two beampaths are
co-aligned. As a convenient check, the HeNe beam partially transmitted
through the microscope slide should strike the trigger photodiode
slightly left of its central region. This small displacement occurs
because the Nd:YAG pulse and HL1's beam do not intercept the microscope
slide's front surface at the same point. This is depicted in Fig. 4.2.

If the trigger photodiode is still positioned to intercept the
Nd:YAG reflection, install an adjustable narrow band pass filter (see
pgs.24,25) in front of the detector. Orient the filter so that it
partially reflects HL1's beam back upon itself. When this is accom-
plished, heavy tape should be used to create a light-tight seal between
the edges of the filter and the detector. The trigger photodiode is now
both fully aligned and isolated from non-1.064μm light. It, and the
microscope slide, must not be further adjusted.

A range of 731.5 cm has been selected as a constant parameter of
all the measurements. This is conveniently half the distance between
the reference plane and the back wall of the laboratory. A piece of
monofilament line, securely attached to the edge of the experimental
table, can be pulled taut and used to mark this range along the Nd:YAG
optic axis. An adjustable flat mirror, positioned at the proper range,
will simulate a target for alignment purposes. This mirror can be used
to point HL1's beam (and the Nd:YAG optic axis) back at an unoccupied
region of the experimental table immediately to the right of the

47

HeNe laser 1
(with adjustments in
both lateral angle
and translation).

OPTIC
AXIS

Nd : YAG
PULSED
LASER

FM-1
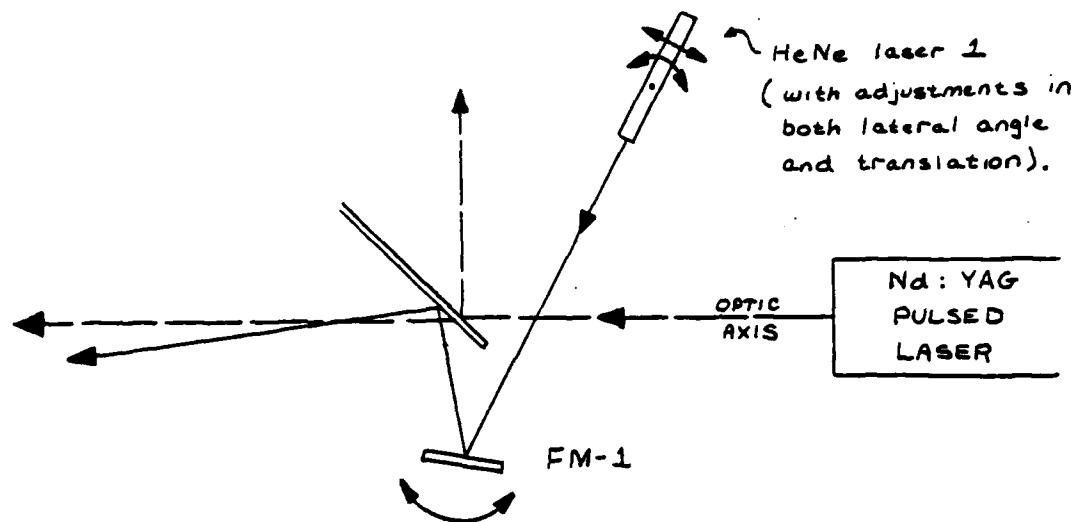
Fig. 4.1.   Schematic for Co-Alignment of HL1 and Nd:YAG Beampaths

MICROSCOPE
SLIDE

DISPLACED BEAMS
AT THE TRIGGER
PHOTODIODE

OPTIC
AXIS

CO-ALIGNED
BEAMPATHS

FRONT SURFACE
OF MICROSCOPE
SLIDE

REAR SURFACE OF
MICROSCOPE SLIDE

FM-1
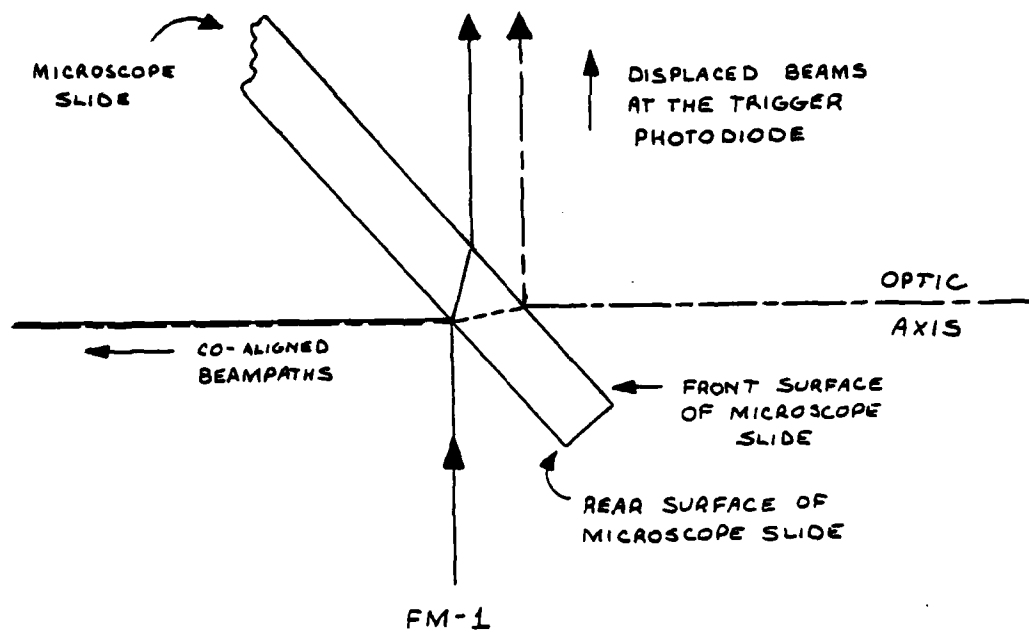
Fig. 4.2.   Displacement of the Reference Beam
at the Trigger Photodiode

microscope slide (see Fig. 2.1). The collecting telescope and the signal photodiode will lie along this new beampath.

The alignment of this focusing telescope and the signal photodiode is, by far, the most complicated part of this total procedure. The first stem requires that a second HeNe laser, to be called "HL2," be installed to the right of the Nd:YAG laser. This HeNe, when adjusted in both position and angle, can be co-aligned with the beam from HL1. The two red beams will thus be traveling in opposite directions down the same optic axis, and will both illuminate the same spot on the target mirror. The telescope now needs to be installed so that its own optic axis is co-aligned with that of HL2. This fine alignment is complete when two criteria are met. The first is that HL2's transmitted beam, although focused by the telescope, must still be co-aligned with the beam from HL1. The second criteria is more subtle. Some element within the telescope partially relects HeNe light. As a result, Newton's rings are produced about the output aperture of HL2. The second criteria requires that these rings be centered on the aperture. When these two criteria are simultaneously met, the telescope is well aligned for a specific focus setting.

Normally, the focus of the telescope should not affect its align-ment. Unfortunately, that is not true of the particular instrument used. The telescope's optic axis, it was discovered, changes slightly in angle as the focus is driven from one extreme to the other. In the interest of time, the telescope's focus setting was optimized; this is described below. Once the focus was optimized, the telescope was re-aligned and then left untouched throughout the course of the LRCS measurements.

The choice of focus setting for the telescope must satisfy two criteria:

1) it must be close enough so that the largest target sphere is within the detector's field of view, and

2) the focus setting must be far enough so that the signal out of the telescope does not overfill the detector.

This second criteria is the more serious, because the sphere size can always be reduced to accomodate a small field of view.

The telescope's output lens is 5.00 mm in diameter but the detector's active region is only 2.54 mm in diameter. Therefore, every effort must first be made to always guarantee that the captured signal that exits the telescope converges at least to this 2.54 mm diameter circular region. Should the signal overfill the detector, the measured LRCS will be erroneously low. A simple criteria exists for identifying which of these two situations exist. In order to implement it, HL2's beam will have to be temporarily blocked by the installation of a signal detector and an appropriate collection of neutral density filters. Once installed and visually centered on the telescope's output, signals can immediately be recorded and displayed on the storage oscilloscope. By maximizing the displayed signals, the photodiode can then be finely aligned in the plane perpendicular to the telescope's optic axis. When this is done, install the -600 mm diverging lens at the Nd:YAG laser's output, and align it in translation and angle by also maximizing the displayed signal. The converging signal that exits the telescope has an ever shrinking spot size as it approaches its own focus. As the detector is further and further removed from the telescope, it captures more and more of this shrinking spot until finally, it measures all of it.

50

Beyond this point, the maximized signal strength remains constant as the detector moves through the converging signal's focus. At the focus itself, a small amount of ringing can be observed on the displayed waveform as a local region of the photodiode is driven non-linearly by the concentrated signal. Knowing these techniques, the maximum telescope focus setting which does not overfill the detector's active region can then be determined. For this setting, the detector's field of view now requires closer examination. This is accomplished using a white index card, which, it is found, is a strong, almost Lambertian scatterer at $\lambda = 1.064 \mu m$. The signal from the index card is much greater than that of the largest sphere but far less than that of an aligned specular mirror. The target mirror should therefore be replaced with the largest sphere which is 1.587 cm in radius and is supported by a specially made lucite rod. Using the detected signal size as a measure of the alignment, adjust the three dimensional location of the sphere to maximize the collected return. When this has been done, one point on the surface of the sphere will intercept both the Nd:YAG's and the telescope's optic axis. Starting inches below the bottom of the sphere, slowly move the edge of the index card up the lucite support rod. As the index card moves within both the spatial limits of the incident pulse and the telescope's field of view, the detected return signal increases dramatically. Fortunately, the field of view is found to just include the 1.587 cm (radius) sphere. This was easily verified by removing the sphere from the lucite rod; the rod, whose position had not changed, contributed a small but distinct reflection that the detector was able to measure. By lowering the rod 1/8 inch, that return disappeared.

The work done so far is generic to all of the measurements. It is at this point in the alignment sequence that a specific target sphere must be properly positioned for measurement purposes. For this reason, all alignment techniques described in the following paragraphs will need to be repeated whenever one sphere is replaced with another.

Procedures Required for the Alignment of Each Sphere. For a telescope with a constant field of view, there is one specific error which grows as the ball size shrinks. That error involves the magnitude of the "background" signal due to the lucite support rod. As smaller and smaller spheres are measured, more and more of the lucite rod is required to enter the telescope's fixed field of view. This is so that each ball can be properly supported in a position centered on the Nd:YAG optic axis. For smaller and smaller spheres the ratio

$$\epsilon = \frac{\text{SIGNAL CONTRIBUTED BY THE ROD}}{\text{SIGNAL CONTRIBUTED BY THE SPHERE}} \tag{36}$$

grows. This is true in spite of the fact that lucite rods of reduced size have been purposely used to support most of the smaller balls. The specific effects described here can be seen by inspecting the data in Chapter V as a function of sphere radius.

The alignment of each ball bearing is complicated by this error. Since the premier technique involves maximizing the return signal amplitude for each adjustment mode, some compensation must be introduced to offset the effect of the lucite rod. The issue is not that the effect of the rod should be measured and then subtracted from the total signal. Instead, the issue is that the sphere will sit much too high,

with respect to the Nd:YAG optic axis, at the completion of the alignment. The solution to this problem involves heavy reliance on HL2. With the signal photodiode removed, HL2's beam focuses through the telescope to a clean, well-defined 1/4" diameter spot at the designated range of 731.5 cm. Since this alignment process is most important for the smaller spheres, the size of the HeNe spot is ideal. They can be easily centered about such a spot. For those ball bearings which are smaller than the 1/4" spot, an examination of the near field shadow will provide sufficient resolution by which to perform the alignment. It should be emphasized that this technique is only 100% valid for adjustments in the vertical axis; this is because unsymmetric reflections occur in the plane containing both the incident and reflected Nd:YAG optic axis (refer to Appendix A). When the sphere has been properly adjusted in elevation, the photodiode should once again be re-installed and aligned to the position of greatest measured return signal. Then, adjustments to the sphere's location in the two remaining axis may be completed. This concludes the preparatory process. Although quite time consuming, the procedures lead to repeatable results provided the sphere has not been re-oriented on the lucite post. This is demonstrated in Chapter V's data section. Before any serious quantitative measurements are recorded, the Nd:YAG laser and the two data recording devices should be allowed to operate for at least one half hour. This warm-up period is merely precautionary.

The Measurement Process

Once the experiment is properly prepared, it is straightforward to conduct. Because of the record of reliable performance earned by the

53

FND-100 photodiode, the primary source of inconsistencies in this process is the Nd:YAG laser. In order to better deal with those variations, 20 measurements will be made under identical conditions for every data point required. Any of the 20 measurements which deviate from the rest of the group by more than 15% will be disregarded. The rest of the group will be statistically averaged to generate the required data point plus or minus its standard deviation.

The characteristic effect of detector noise on the measured signals can now be calculated. The performance characteristics of the FND-100 photodiode are presented in Table 2.2. The definition of Noise Equivalent Power (NEP) is

$$NEP = \frac{(E_e)_{RMS} \times A_d}{\left(v_{sig} / v_{noise} \right)_{RMS}} \tag{37}$$

where

$(E_e)_{RMS}$ = the incident irradiance (RMS value)
A_d = active area of the detector
   = 5.1 mm²
$\left(v_{sig} / v_{noise} \right)_{RMS}$ = the RMS Signal-to-Noise Ratio

(Hengehold, 1985:99). Since this detector's NEP is quoted to be 2.9 × 10^{-13} Watts, the effective signal-to-noise ratio is

$$\left(\frac{v_{sig}}{v_{noise}} \right)_{RMS} = (3.4482 \times 10^{12}) \times P \tag{38}$$

where

P = incident Power (in units of watts) on the detector (RMS value)

Although the power, P, is not known, it should be fairly large because

54

of the short pulsewidth. The signal-to-noise ratio should therefore be tremendous in size; furthermore, the very small dark current generated (less than 100 nanoamperes) will not cause an error which is even measurable on the lower millivolt scales. The largest error introduced to the measurement by this choice of detector is actually found in the form of the internal amplifiers which support the data recording instruments. These types of errors are not pertinent to the experiment, though; they primarily affect the response time of the trace and, in fact, have little effect on the displayed amplitudes (when in the millivolt range) (Tektronix, 1983:1-11).

For every optical pulse emitted by the laser, a temporal profile is recorded on the Storage Oscilloscope. An example is presented in Fig. 4.3. It represents a return from a .635 cm radius ball bearing and would be documented as having a peak amplitude of 640 ± 20 millivolts. A similar profile from the EG&G Signal processor is provided in Fig. 4.4.
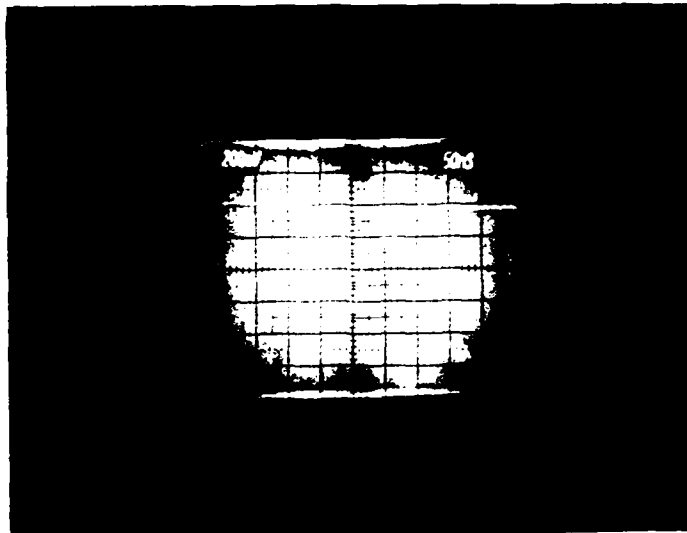
Fig. 4.3. A Valid Return Signal From a 0.635 cm Radius Sphere

(Profiled on a Tektronix Storage Oscilloscope)
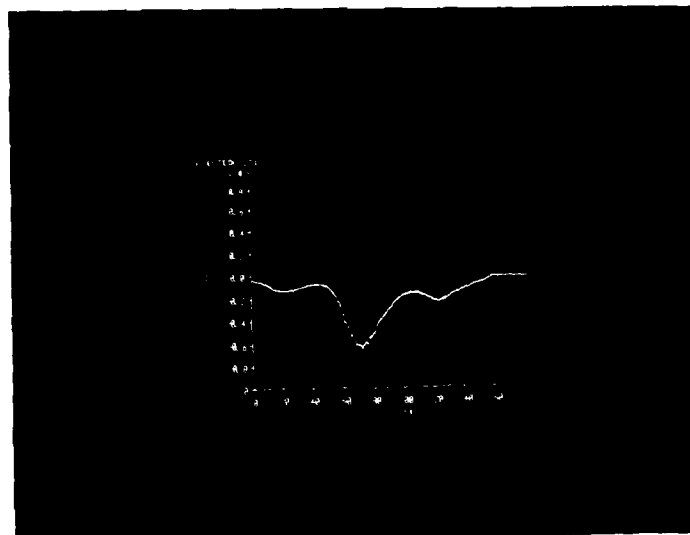
Fig. 4.4. A Valid Return Signal From a 0.635 cm Radius Sphere

(Profiled on an EG&G Signal Processor)

V. Experimental Measurements and Analysis

This chapter is organized into two major sections. The first section presents all of the measured data from the experiment. This includes the maximum signal amplitudes caused by each of the 13 target spheres, together with their supporting rods. Furthermore, the effect of the rods, once the spheres have been removed, is also documented. The second section comprises an analysis of the data which is tabulated in the first section. A comparison will be made between these experimental results and the theoretical predictions that are listed in Appendix B.

Measurements

The measurements are presented in Tables 5.1 through 5.13. Each table contains eighty different measurements, divided into four groups of twenty, and each of the eighty measurements are made for the exact same position of the lucite support rod. This rod, while holding any one particular sphere, is aligned in a position that is unique to that sphere. The first three columns in Tables 5.1 through 5.13 each represent a new orientation of the ball bearing on the rod. The values within any column, therefore, change only as the laser performance changes. The extent that the laser's output intensity has varied is reflected by the standard deviation calculated at the bottom of each column. The mean values for each column are also calculated and are listed at the bottom of each table. Within any particular table, a comparison of the first three column's average values provides some

TABLE 5.1.

Measurement of 1.587 cm Radius Sphere (in Volts)

(sphere supported by rod #1)

	1st Orientation	2nd Orientation	3rd Orientation	The Rod Alone
measured values	2.68 ± .05	2.79 ± .05	2.47 ± .05	0.140 ± .005
	2.72 ± .05	2.81 ± .05	2.51 ± .05	0.142 ± .005
	2.71 ± .05	2.77 ± .05	2.48 ± .05	0.137 ± .005
	2.69 ± .05	2.76 ± .05	2.46 ± .05	0.139 ± .005
	2.63 ± .05	2.77 ± .05	2.48 ± .05	0.140 ± .005
	2.70 ± .05	2.72 ± .05	2.49 ± .05	0.142 ± .005
	2.63 ± .05	2.73 ± .05	2.45 ± .05	0.145 ± .005
	2.70 ± .05	2.71 ± .05	2.52 ± .05	0.142 ± .005
	2.71 ± .05	2.75 ± .05	2.47 ± .05	0.141 ± .005
	2.70 ± .05	2.74 ± .05	2.47 ± .05	0.142 ± .005
	2.70 ± .05	2.74 ± .05	2.45 ± .05	0.142 ± .005
	2.67 ± .05	2.74 ± .05	2.49 ± .05	0.141 ± .005
	2.69 ± .05	2.74 ± .05	2.51 ± .05	0.140 ± .005
	2.72 ± .05	2.75 ± .05	2.50 ± .05	0.139 ± .005
	2.70 ± .05	2.77 ± .05	2.48 ± .05	0.137 ± .005
	2.65 ± .05	2.80 ± .05	2.47 ± .05	0.138 ± .005
	2.69 ± .05	2.79 ± .05	2.48 ± .05	0.142 ± .005
	2.68 ± .05	2.79 ± .05	2.48 ± .05	0.143 ± .005
	2.70 ± .05	2.81 ± .05	2.50 ± .05	0.140 ± .005
	2.69 ± .05	2.80 ± .05	2.49 ± .05	0.137 ± .005
mean value	2.688	2.764	2.482	0.140
standard deviation	0.025	0.029	0.019	0.002

TABLE 5.2.

Measurements of 1.349 cm Radius Sphere (in Volts)

(sphere supported by rod #1)

	1st Orientation	2nd Orientation	3rd Orientation	The Rod Alone
measured values	2.18 ± .05	2.12 ± .05	2.19 ± .05	0.225 ± .005
	2.17 ± .05	2.15 ± .05	2.17 ± .05	0.224 ± .005
	2.20 ± .05	2.11 ± .05	2.17 ± .05	0.221 ± .005
	2.20 ± .05	2.14 ± .05	2.19 ± .05	0.216 ± .005
	2.21 ± .05	2.13 ± .05	2.20 ± .05	0.215 ± .005
	2.20 ± .05	2.12 ± .05	2.25 ± .05	0.218 ± .005
	2.19 ± .05	2.12 ± .05	2.19 ± .05	0.218 ± .005
	2.17 ± .05	2.11 ± .05	2.18 ± .05	0.215 ± .005
	2.20 ± .05	2.12 ± .05	2.20 ± .05	0.220 ± .005
	2.19 ± .05	2.14 ± .05	2.19 ± .05	0.221 ± .005
	2.21 ± .05	2.12 ± .05	2.17 ± .05	0.217 ± .005
	2.24 ± .05	2.13 ± .05	2.20 ± .05	0.216 ± .005
	2.22 ± .05	2.09 ± .05	2.22 ± .05	0.215 ± .005
	2.21 ± .05	2.10 ± .05	2.23 ± .05	0.216 ± .005
	2.22 ± .05	2.11 ± .05	2.18 ± .05	0.216 ± .005
	2.20 ± .05	2.14 ± .05	2.19 ± .05	0.219 ± .005
	2.21 ± .05	2.12 ± .05	2.19 ± .05	0.221 ± .005
	2.21 ± .05	2.13 ± .05	2.24 ± .05	0.219 ± .005
	2.21 ± .05	2.12 ± .05	2.19 ± .05	0.218 ± .005
	2.20 ± .05	2.10 ± .05	2.21 ± .05	0.216 ± .005
mean value	2.202	2.121	2.197	0.218
standard deviation	0.016	0.015	0.022	0.003

TABLE 5.3.

Measurements of 1.191 cm Radius Sphere (in Volts)

(sphere supported by rod #1)

	1st Orientation	2nd Orientation	3rd Orientation	The Rod Alone
measured values	2.04 ± .05	2.00 ± .05	2.11 ± .05	0.276 ± .005
	2.05 ± .05	2.05 ± .05	2.10 ± .05	0.275 ± .005
	2.05 ± .05	2.04 ± .05	2.13 ± .05	0.275 ± .005
	2.03 ± .05	2.02 ± .05	2.07 ± .05	0.272 ± .005
	2.05 ± .05	2.03 ± .05	2.07 ± .05	0.273 ± .005
	2.05 ± .05	2.01 ± .05	2.09 ± .05	0.272 ± .005
	2.04 ± .05	2.00 ± .05	2.08 ± .05	0.272 ± .005
	2.02 ± .05	2.01 ± .05	2.12 ± .05	0.271 ± .005
	2.05 ± .05	2.01 ± .05	2.11 ± .05	0.274 ± .005
	2.05 ± .05	2.03 ± .05	2.13 ± .05	0.271 ± .005
	2.02 ± .05	2.00 ± .05	2.12 ± .05	0.269 ± .005
	2.03 ± .05	2.00 ± .05	2.09 ± .05	0.270 ± .005
	2.05 ± .05	1.98 ± .05	2.08 ± .05	0.268 ± .005
	2.06 ± .05	2.02 ± .05	2.08 ± .05	0.269 ± .005
	2.06 ± .05	2.03 ± .05	2.09 ± .05	0.268 ± .005
	2.05 ± .05	2.01 ± .05	2.08 ± .05	0.267 ± .005
	2.06 ± .05	2.02 ± .05	2.10 ± .05	0.271 ± .005
	2.01 ± .05	2.01 ± .05	2.11 ± .05	0.270 ± .005
	2.05 ± .05	2.04 ± .05	2.09 ± .05	0.272 ± .005
	2.05 ± .05	2.04 ± .05	2.08 ± .05	0.271 ± .005
mean value	2.043	2.017	2.096	0.271
standard deviation	0.014	0.017	0.018	0.002

TABLE 5.4.

Measurements of 0.952 cm Radius Sphere (in Volts)

(sphere supported by rod #1)

	1st Orientation	2nd Orientation	3rd Orientation	The Rod Alone
measured values	1.50 ± .05	1.52 ± .05	1.58 ± .05	0.36 ± .01
	1.52 ± .05	1.53 ± .05	1.60 ± .05	0.36 ± .01
	1.52 ± .05	1.55 ± .05	1.59 ± .05	0.36 ± .01
	1.50 ± .05	1.56 ± .05	1.59 ± .05	0.35 ± .01
	1.51 ± .05	1.56 ± .05	1.58 ± .05	0.36 ± .01
	1.55 ± .05	1.55 ± .05	1.53 ± .05	0.35 ± .01
	1.54 ± .05	1.55 ± .05	1.52 ± .05	0.35 ± .01
	1.53 ± .05	1.55 ± .05	1.55 ± .05	0.35 ± .01
	1.53 ± .05	1.50 ± .05	1.56 ± .05	0.36 ± .01
	1.54 ± .05	1.53 ± .05	1.56 ± .05	0.35 ± .01
	1.54 ± .05	1.55 ± .05	1.52 ± .05	0.35 ± .01
	1.53 ± .05	1.53 ± .05	1.57 ± .05	0.35 ± .01
	1.50 ± .05	1.52 ± .05	1.56 ± .05	0.36 ± .01
	1.52 ± .05	1.50 ± .05	1.57 ± .05	0.35 ± .01
	1.54 ± .05	1.51 ± .05	1.61 ± .05	0.35 ± .01
	1.55 ± .05	1.49 ± .05	1.52 ± .05	0.35 ± .01
	1.51 ± .05	1.48 ± .05	1.51 ± .05	0.35 ± .01
	1.57 ± .05	1.51 ± .05	1.55 ± .05	0.35 ± .01
	1.56 ± .05	1.52 ± .05	1.56 ± .05	0.35 ± .01
	1.56 ± .05	1.50 ± .05	1.58 ± .05	0.35 ± .01
mean value	1.531	1.525	1.560	0.353
standard deviation	0.020	0.024	0.028	0.004

TABLE 5.5.

Measurements of 0.873 cm Radius Sphere (in Volts)

(sphere supported by rod #1)

	1st Orientation	2nd Orientation	3rd Orientation	The Rod Alone
measured values	1.32 ± .05	1.26 ± .05	1.32 ± .05	0.38 ± .01
	1.33 ± .05	1.29 ± .05	1.30 ± .05	0.38 ± .01
	1.35 ± .05	1.31 ± .05	1.30 ± .05	0.38 ± .01
	1.29 ± .05	1.30 ± .05	1.31 ± .05	0.37 ± .01
	1.32 ± .05	1.29 ± .05	1.32 ± .05	0.37 ± .01
	1.33 ± .05	1.25 ± .05	1.35 ± .05	0.38 ± .01
	1.37 ± .05	1.28 ± .05	1.32 ± .05	0.38 ± .01
	1.37 ± .05	1.26 ± .05	1.31 ± .05	0.38 ± .01
	1.38 ± .05	1.25 ± .05	1.27 ± .05	0.38 ± .01
	1.34 ± .05	1.25 ± .05	1.29 ± .05	0.37 ± .01
	1.37 ± .05	1.26 ± .05	1.29 ± .05	0.38 ± .01
	1.37 ± .05	1.28 ± .05	1.30 ± .05	0.38 ± .01
	1.37 ± .05	1.33 ± .05	1.33 ± .05	0.37 ± .01
	1.31 ± .05	1.28 ± .05	1.30 ± .05	0.38 ± .01
	1.37 ± .05	1.27 ± .05	1.31 ± .05	0.38 ± .01
	1.36 ± .05	1.26 ± .05	1.30 ± .05	0.38 ± .01
	1.32 ± .05	1.23 ± .05	1.30 ± .05	0.38 ± .01
	1.36 ± .05	1.26 ± .05	1.29 ± .05	0.37 ± .01
	1.35 ± .05	1.25 ± .05	1.32 ± .05	0.38 ± .01
	1.35 ± .05	1.26 ± .05	1.30 ± .05	0.38 ± .01
mean value	1.346	1.271	1.306	0.377
standard deviation	0.025	0.023	0.017	0.004

TABLE 5.6.

Measurements of 0.794 cm Radius Sphere (in Volts)

(sphere supported by rod #2)

	1st Orientation	2nd Orientation	3rd Orientation	The Rod Alone
measured values	0.92 ± .02	0.93 ± .02	0.90 ± .02	0.091 ± .002
	0.94 ± .02	0.92 ± .02	0.87 ± .02	0.092 ± .002
	0.93 ± .02	0.91 ± .02	0.91 ± .02	0.092 ± .002
	0.94 ± .02	0.91 ± .02	0.92 ± .02	0.091 ± .002
	0.94 ± .02	0.91 ± .02	0.91 ± .02	0.092 ± .002
	0.90 ± .02	0.93 ± .02	0.93 ± .02	0.094 ± .002
	0.93 ± .02	0.94 ± .02	0.93 ± .02	0.092 ± .002
	0.91 ± .02	0.93 ± .02	0.91 ± .02	0.093 ± .002
	0.90 ± .02	0.93 ± .02	0.92 ± .02	0.094 ± .002
	0.90 ± .02	0.92 ± .02	0.91 ± .02	0.093 ± .002
	0.91 ± .02	0.91 ± .02	0.91 ± .02	0.094 ± .002
	0.92 ± .02	0.91 ± .02	0.90 ± .02	0.093 ± .002
	0.91 ± .02	0.90 ± .02	0.92 ± .02	0.093 ± .002
	0.93 ± .02	0.94 ± .02·	0.90 ± .02	0.091 ± .002
	0.94 ± .02	0.91 ± .02	0.91 ± .02	0.090 ± .002
	0.94 ± .02	0.94 ± .02	0.93 ± .02	0.091 ± .002
	0.96 ± .02	0.93 ± .02	0.91 ± .02	0.092 ± .002
	0.91 ± .02	0.95 ± .02	0.90 ± .02	0.092 ± .002
	0.92 ± .02	0.97 ± .02	0.90 ± .02	0.091 ± .002
	0.91 ± .02	0.92 ± .02	0.91 ± .02	0.092 ± .002
mean value	0.923	0.925	0.910	0.0921
standard deviation	0.016	0.016	0.013	0.0011

TABLE 5.7.

Measurements of 0.635 cm Radius Sphere (in Volts)

(sphere supported by rod #2)

	1st Orientation	2nd Orientation	3rd Orientation	The Rod Alone
measured values	0.62 ± .02	0.63 ± .02	0.61 ± .02	0.109 ± .002
	0.62 ± .02	0.62 ± .02	0.62 ± .02	0.103 ± .002
	0.65 ± .02	0.64 ± .02	0.62 ± .02	0.107 ± .002
	0.64 ± .02	0.62 ± .02	0.62 ± .02	0.106 ± .002
	0.65 ± .02	0.62 ± .02	0.64 ± .02	0.107 ± .002
	0.64 ± .02	0.63 ± .02	0.65 ± .02	0.106 ± .002
	0.65 ± .02	0.60 ± .02	0.66 ± .02	0.106 ± .002
	0.65 ± .02	0.61 ± .02	0.64 ± .02	0.104 ± .002
	0.64 ± .02	0.65 ± .02	0.66 ± .02	0.107 ± .002
	0.66 ± .02	0.64 ± .02	0.65 ± .02	0.108 ± .002
	0.64 ± .02	0.65 ± .02	0.64 ± .02	0.106 ± .002
	0.63 ± .02	0.64 ± .02	0.65 ± .02	0.106 ± .002
	0.63 ± .02	0.63 ± .02	0.63 ± .02	0.107 ± .002
	0.66 ± .02	0.63 ± .02	0.64 ± .02	0.106 ± .002
	0.65 ± .02	0.64 ± .02	0.65 ± .02	0.105 ± .002
	0.64 ± .02	0.63 ± .02	0.64 ± .02	0.105 ± .002
	0.60 ± .02	0.62 ± .02	0.65 ± .02	0.105 ± .002
	0.62 ± .02	0.61 ± .02	0.64 ± .02	0.106 ± .002
	0.62 ± .02	0.64 ± .02	0.63 ± .02	0.108 ± .002
	0.63 ± .02	0.63 ± .02	0.63 ± .02	0.105 ± .002
mean value	0.637	0.629	0.638	0.1061
standard deviation	0.015	0.013	0.013	0.0014

64

TABLE 5.8

Measurements of 0.556 cm Radius Sphere (in Volts)

(sphere supported by rod #2)

	1st Orientation	2nd Orientation	3rd Orientation	The Rod Alone
measured values	0.51 ± .02	0.48 ± .02	0.51 ± .02	0.130 ± .002
	0.53 ± .02	0.47 ± .02	0.52 ± .02	0.128 ± .002
	0.54 ± .02	0.47 ± .02	0.56 ± .02	0.128 ± .002
	0.55 ± .02	0.51 ± .02	0.55 ± .02	0.127 ± .002
	0.55 ± .02	0.49 ± .02	0.55 ± .02	0.130 ± .002
	0.53 ± .02	0.48 ± .02	0.55 ± .02	0.129 ± .002
	0.54 ± .02	0.47 ± .02	0.55 ± .02	0.128 ± .002
	0.55 ± .02	0.49 ± .02	0.55 ± .02	0.128 ± .002
	0.53 ± .02	0.49 ± .02	0.56 ± .02	0.129 ± .002
	0.53 ± .02	0.49 ± .02	0.52 ± .02	0.131 ± .002
	0.54 ± .02	0.50 ± .02	0.51 ± .02	0.130 ± .002
	0.52 ± .02	0.51 ± .02	0.52 ± .02	0.129 ± .002
	0.53 ± .02	0.49 ± .02	0.53 ± .02	0.127 ± .002
	0.50 ± .02	0.47 ± .02	0.53 ± .02	0.130 ± .002
	0.54 ± .02	0.46 ± .02	0.55 ± .02	0.130 ± .002
	0.51 ± .02	0.55 ± .02	0.54 ± .02	0.128 ± .002
	0.51 ± .02	0.48 ± .02	0.55 ± .02	0.128 ± .002
	0.53 ± .02	0.50 ± .02	0.51 ± .02	0.127 ± .002
	0.52 ± .02	0.51 ± .02	0.52 ± .02	0.128 ± .002
	0.53 ± .02	0.50 ± .02	0.51 ± .02	0.128 ± .002
mean value	0.529	0.491	0.534	0.1286
standard deviation	0.014	0.019	0.018	0.0012

TABLE 5.9.

Measurements of 0.476 cm Radius Sphere (in Volts)

(sphere supported by rod #3)

	1st Orientation	2nd Orientation	3rd Orientation	The Rod Alone
measured values	0.38 ± .01	0.36 ± .01	0.34 ± .01	0.054 ± .001
	0.36 ± .01	0.35 ± .01	0.33 ± .01	0.057 ± .001
	0.37 ± .01	0.37 ± .01	0.34 ± .01	0.056 ± .001
	0.37 ± .01	0.35 ± .01	0.34 ± .01	0.056 ± .001
	0.37 ± .01	0.36 ± .01	0.35 ± .01	0.057 ± .001
	0.35 ± .01	0.38 ± .01	0.33 ± .01	0.056 ± .001
	0.36 ± .01	0.35 ± .01	0.35 ± .01	0.056 ± .001
	0.36 ± .01	0.48*	0.34 ± .01	0.056 ± .001
	0.36 ± .01	0.36 ± .01	0.34 ± .01	0.057 ± .001
	0.35 ± .01	0.35 ± .01	0.34 ± .01	0.055 ± .001
	0.37 ± .01	0.35 ± .01	0.36 ± .01	0.056 ± .001
	0.36 ± .01	0.35 ± .01	0.34 ± .01	0.055 ± .001
	0.37 ± .01	0.37 ± .01	0.35 ± .01	0.055 ± .001
	0.37 ± .01	0.37 ± .01	0.33 ± .01	0.057 ± .001
	0.36 ± .01	0.35 ± .01	0.33 ± .01	0.056 ± .001
	0.35 ± .01	0.36 ± .01	0.34 ± .01	0.055 ± .001
	0.35 ± .01	0.36 ± .01	0.35 ± .01	0.056 ± .001
	0.37 ± .01	0.35 ± .01	0.34 ± .01	0.055 ± .001
	0.38 ± .01	0.36 ± .01	0.36 ± .01	0.056 ± .001
	0.36 ± .01	0.36 ± .01	0.34 ± .01	0.056 ± .001
mean value	0.363	0.358	0.342	0.0558
standard deviation	0.009	0.009	0.009	0.0008

*. . . Invalid Data Point

TABLE 5.10

Measurement of 0.397 cm Radius Sphere (in Volts)

(sphere supported by rod #3)

	1st Orientation	2nd Orientation	3rd Orientation	The Rod Alone
measured values	0.272 ± .005	0.255 ± .005	0.267 ± .005	0.064 ± .002
	0.277 ± .005	0.259 ± .005	0.270 ± .005	0.061 ± .002
	0.283 ± .005	0.268 ± .005	0.271 ± .005	0.062 ± .002
	0.281 ± .005	0.271 ± .005	0.273 ± .005	0.062 ± .002
	0.276 ± .005	0.265 ± .005	0.274 ± .005	0.064 ± .002
	0.267 ± .005	0.268 ± .005	0.271 ± .005	0.065 ± .002
	0.269 ± .005	0.267 ± .005	0.276 ± .005	0.064 ± .002
	0.274 ± .005	0.271 ± .005	0.277 ± .005	0.062 ± .002
	0.275 ± .005	0.272 ± .005	0.274 ± .005	0.063 ± .002
	0.271 ± .005	0.264 ± .005	0.272 ± .005	0.063 ± .002
	0.278 ± .005	0.261 ± .005	0.269 ± .005	0.062 ± .002
	0.281 ± .005	0.261 ± .005	0.268 ± .005	0.061 ± .002
	0.284 ± .005	0.268 ± .005	0.270 ± .005	0.059 ± .002
	0.283 ± .005	0.269 ± .005	0.272 ± .005	0.062 ± .002
	0.288 ± .005	0.271 ± .005	0.274 ± .005	0.064 ± .002
	0.271 ± .005	0.275 ± .005	0.275 ± .005	0.064 ± .002
	0.275 ± .005	0.275 ± .005	0.271 ± .005	0.064 ± .002
	0.276 ± .005	0.272 ± .005	0.273 ± .005	0.063 ± .002
	0.265 ± .005	0.268 ± .005	0.272 ± .005	0.063 ± .002
	0.264 ± .005	0.270 ± .005	0.269 ± .005	0.061 ± .002
mean value	0.2755	0.2675	0.2719	0.0626
standard deviation	0.00641	0.00515	0.00258	0.0014

TABLE 5.11.

Measurement of 0.317 cm Radius Sphere (in Volts)

(sphere supported by rod #3)

	1st Orientation	2nd Orientation	3rd Orientation	The Rod Alone
measured values	0.208 ± .005	0.220 ± .005	0.191 ± .005	0.072 ± .002
	0.210 ± .005	0.218 ± .005	0.196 ± .005	0.072 ± .002
	0.205 ± .005	0.219 ± .005	0.195 ± .005	0.070 ± .002
	0.205 ± .005	0.219 ± .005	0.196 ± .005	0.071 ± .002
	0.205 ± .005	0.226 ± .005	0.198 ± .005	0.070 ± .002
	0.207 ± .005	0.219 ± .005	0.189 ± .005	0.071 ± .002
	0.210 ± .005	0.218 ± .005	0.192 ± .005	0.069 ± .002
	0.212 ± .005	0.221 ± .005	0.193 ± .005	0.071 ± .002
	0.214 ± .005	0.224 ± .005	0.196 ± .005	0.072 ± .002
	0.205 ± .005	0.227 ± .005	0.199 ± .005	0.070 ± .002
	0.198 ± .005	0.226 ± .005	0.205 ± .005	0.070 ± .002
	0.210 ± .005	0.222 ± .005	0.196 ± .005	0.071 ± .002
	0.206 ± .005	0.219 ± .005	0.197 ± .005	0.073 ± .002
	0.209 ± .005	0.224 ± .005	0.191 ± .005	0.072 ± .002
	0.205 ± .005	0.216 ± .005	0.188 ± .005	0.073 ± .002
	0.215 ± .005	0.211 ± .005	0.194 ± .005	0.071 ± .002
	0.206 ± .005	0.217 ± .005	0.199 ± .005	0.070 ± .002
	0.204 ± .005	0.221 ± .005	0.203 ± .005	0.071 ± .002
	0.204 ± .005	0.228 ± .005	0.202 ± .005	0.072 ± .002
	0.200 ± .005	0.221 ± .005	0.197 ± .005	0.070 ± .002
mean value	0.2065	0.2108	0.1958	0.0710
standard deviation	0.0042	0.0041	0.0044	0.0011

68

TABLE 5.12.

Measurement of 0.238 cm Radius Sphere (in Volts)

(sphere supported by rod #4)

	1st Orientation	2nd Orientation	3rd Orientation	The Rod Alone
measured values	0.076 ± .002	0.075 ± .002	0.079 ± .002	0.024 ± .001
	0.076 ± .002	0.076 ± .002	0.079 ± .002	0.024 ± .001
	0.077 ± .002	0.076 ± .002	0.079 ± .002	0.024 ± .001
	0.077 ± .002	0.075 ± .002	0.078 ± .002	0.024 ± .001
	0.076 ± .002	0.074 ± .002	0.079 ± .002	0.024 ± .001
	0.077 ± .002	0.075 ± .002	0.079 ± .002	0.025 ± .001
	0.077 ± .002	0.076 ± .002	0.078 ± .002	0.024 ± .001
	0.077 ± .002	0.077 ± .002	0.078 ± .002	0.024 ± .001
	0.076 ± .002	0.076 ± .002	0.079 ± .002	0.024 ± .001
	0.076 ± .002	0.076 ± .002	0.079 ± .002	0.024 ± .001
	0.077 ± .002	0.076 ± .002	0.079 ± .002	0.024 ± .001
	0.077 ± .002	0.075 ± .002	0.080 ± .002	0.024 ± .001
	0.076 ± .002	0.076 ± .002	0.079 ± .002	0.024 ± .001
	0.077 ± .002	0.077 ± .002	0.079 ± .002	0.024 ± .001
	0.077 ± .002	0.075 ± .002	0.079 ± .002	0.024 ± .001
	0.077 ± .002	0.075 ± .002	0.078 ± .002	0.024 ± .001
	0.077 ± .002	0.075 ± .002	0.079 ± .002	0.024 ± .001
	0.076 ± .002	0.075 ± .002	0.079 ± .002	0.024 ± .001
	0.077 ± .002	0.076 ± .002	0.078 ± .002	0.024 ± .001
	0.077 ± .002	0.076 ± .002	0.078 ± .002	0.024 ± .001
mean values	0.0766	0.0756	0.0787	0.0241
standard deviation	0.0005	0.0007	0.0005	0.0002

TABLE 5.13.

Measurements of 0.159 cm Radius Sphere (in Volts)

(sphere supported by rod #4)

	1st Orientation	2nd Orientation	3rd Orientation	The Rod Alone
measured values	0.035 ± .001	0.034 ± .001	0.035 ± .001	0.026 ± .001
	0.035 ± .001	0.034 ± .001	0.035 ± .001	0.025 ± .001
	0.036 ± .001	0.034 ± .001	0.034 ± .001	0.026 ± .001
	0.034 ± .001	0.035 ± .001	0.035 ± .001	0.026 ± .001
	0.035 ± .001	0.034 ± .001	0.034 ± .001	0.025 ± .001
	0.035 ± .001	0.034 ± .001	0.034 ± .001	0.026 ± .001
	0.035 ± .001	0.034 ± .001	0.034 ± .001	0.026 ± .001
	0.035 ± .001	0.034 ± .001	0.035 ± .001	0.026 ± .001
	0.035 ± .001	0.034 ± .001	0.034 ± .001	0.026 ± .001
	0.034 ± .001	0.035 ± .001	0.034 ± .001	0.025 ± .001
	0.035 ± .001	0.034 ± .001	0.035 ± .001	0.026 ± .001
	0.035 ± .001	0.034 ± .001	0.035 ± .001	0.026 ± .001
	0.035 ± .001	0.034 ± .001	0.034 ± .001	0.026 ± .001
	0.036 ± .001	0.034 ± .001	0.035 ± .001	0.025 ± .001
	0.035 ± .001	0.034 ± .001	0.035 ± .001	0.026 ± .001
	0.035 ± .001	0.034 ± .001	0.035 ± .001	0.026 ± .001
	0.035 ± .001	0.035 ± .001	0.035 ± .001	0.026 ± .001
	0.035 ± .001	0.035 ± .001	0.035 ± .001	0.025 ± .001
	0.036 ± .001	0.034 ± .001	0.035 ± .001	0.026 ± .001
	0.035 ± .001	0.034 ± .001	0.034 ± .001	0.026 ± .001
mean values	0.0351	0.0342	0.0346	0.0257
standard deviation	0.0005	0.0004	0.0005	0.0004

insight into the uniformity of the specific sphere's surface. The fourth column in each of these tables measures the effect of just the rod, once the sphere has been removed.

In order to better comprehend the repeatability of the alignment process described in Chapter IV, certain measurements were made three additional times of the 0.635 cm radius sphere. In all three cases, the sphere's orientation on its support rod was not changed in any manner. In each case, however, the rods (and the balls resting on them) were mis-aligned in all three axis, and then re-aligned, before any measurements were made. The results of these independent measurements are featured in Table 5.14.

Analysis of the Results

In order for these results to be easily compared with the theoretical predictions of Appendix B, Tables 5.1 through 5.13 need to be condensed into a more palatable form. This is accomplished in Table 5.15. Here, the difference between the largest mean value for both rod and sphere, and the mean value for the rod alone, is tabulated. The choice of the "largest" mean value is predicated on the following rationale. If the sphere's surface is perfect, these "mean" terms will always be statistically equal. With a large enough number of repeated measurements, the change in laser performance will always average out. But no part of the sphere's surface is perfect; each mean value represents the performance of a local surface element on the sphere. By choosing the "largest" mean value, only the best of these three localized regions is considered in the comparison. As it turns out, the "best" of the three regions may not be very good at all. Looking

TABLE 5.14.

Measurements Designed to Test the Experiment's

Alignment Repeatability (0.635 cm radius ball used)

	1st Alignment	1st Re-Alignment	2nd Re-Alignment
measured values	0.62 ± .02	0.63 ± .02	0.65 ± .02
	0.64 ± .02	0.63 ± .02	0.63 ± .02
	0.64 ± .02	0.64 ± .02	0.62 ± .02
	0.63 ± .02	0.65 ± .02	0.61 ± .02
	0.64 ± .02	0.62 ± .02	0.64 ± .02
	0.65 ± .02	0.63 ± .02	0.64 ± .02
	0.62 ± .02	0.61 ± .02	0.65 ± .02
	0.61 ± .02	0.64 ± .02	0.64 ± .02
	0.65 ± .02	0.63 ± .02	0.66 ± .02
	0.63 ± .02	0.62 ± .02	0.61 ± .02
	0.62 ± .02	0.62 ± .02	0.60 ± .02
	0.64 ± .02	0.61 ± .02	0.63 ± .02
	0.65 ± .02	0.63 ± .02	0.63 ± .02
	0.65 ± .02	0.64 ± .02	0.64 ± .02
	0.64 ± .02	0.65 ± .02	0.62 ± .02
	0.62 ± .02	0.64 ± .02	0.63 ± .02
	0.63 ± .02	0.65 ± .02	0.62 ± .02
	0.65 ± .02	0.63 ± .02	0.63 ± .02
	0.63 ± .02	0.62 ± .02	0.63 ± .02
	0.64 ± .02	0.64 ± .02	0.63 ± .02
mean value	0.635	0.632	0.631
standard deviation	0.012	0.012	0.012

TABLE 5.15.

Measured Signal Strengths From 13 Spherical Targets and the

Corresponding Predictions From Geometric Optics

sphere's radius (cm)	measured voltage (the largest mean value) (V)	effect of rod (its mean value) (V)	Net signal from just the sphere (V)	predicted Voltage (V)
1.587	2.764	0.140	2.624	3.561
1.349	2.202	0.218	1.984	2.574
1.191	2.096	0.271	1.825	2.006
0.952	1.560	0.353	1.207	1.282
0.873	1.346	0.377	0.969	1.078
0.794	0.925	0.092	0.833	0.892
0.635	0.638	0.106	0.532	0.571
0.556	0.534	0.128	0.406	0.438
0.476	0.363	0.056	0.307	0.321
0.397	0.275	0.063	0.213	0.223
0.317	0.211	0.071	0.140	0.142
0.238	0.079	0.024	0.055	0.080
0.159	0.035	0.026	0.009	0.036

specifically at data in Table 5.1, the three different orientations of the 1.587 cm sphere resulted in significant variations in captured signal. If the lowest of the three values (i.e., 2.482 V) is the result of some local damage to the sphere's surface, then it certainly should not be considered. Damage to some of the spheres is present in the form of corrosion. In particular, 5 of the 13 spheres have suffered from pitting in their surfaces which is visible to the naked eye. This was known before any of the measurements were conducted, and every attempt was made to orient these surface defects as far from the Nd:YAG optic axis as possible. The most severe damage is present on the 1.587 cm sphere (see Fig. 5.1). This photo, at a magnification of ~57X, details some of the less massive reaction sites on the surface. The smaller sites were chosen for documentation because of two reasons:

1) there was much higher contrast in these photos than there was in photos of serious damage in which most of the surface was black.

2) The small sites are probably more significant since the more extensive problem areas were purposefully kept far from the optic axis. As a convenient reference, Fig 5.2 is provided, also at a magnification of ~57X. The separation between adjacent tick marks is 0.1 mm. Using this scale, the damage in Fig. 5.1 is found to occupy greater than 0.05 mm^2 of surface area within this camera's field of view. Even more significantly, Fig 5.1 exposes the random dense array of deep gouges and scratches which mar the surface. These were most likely created during the cleaning process. As chemical residue from the corrosion separated from the sphere during cleaning, it served to act as an abrasive under the alcohol soaked lens tissue. Although a more quantitative evaluation of the damage was not possible, this sphere certainly has a high
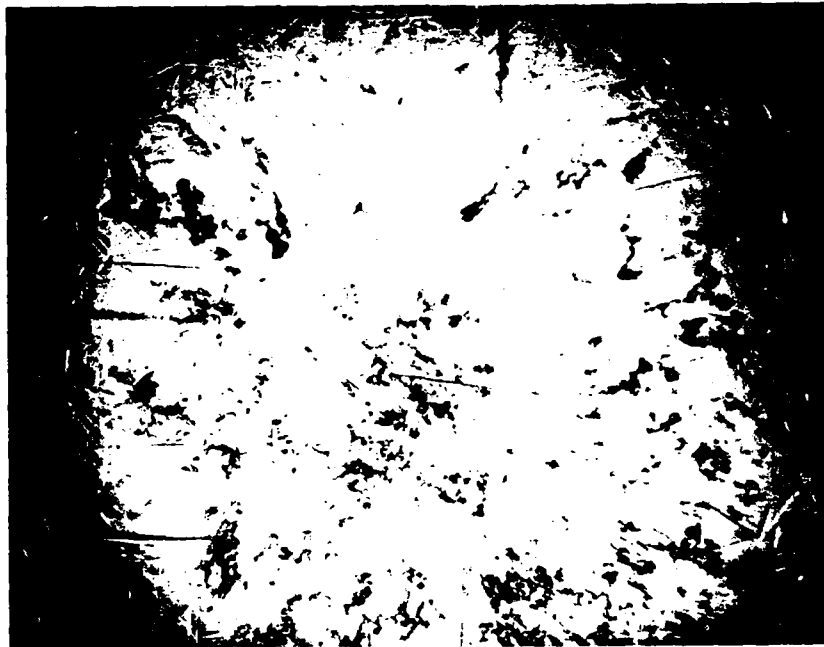
74

Fig. 5.1. Representative Photo of Mild Surface Corrosion on 1.537 cm
Sphere (magnification ≐ 57X).

scattering surface. Even if no corrosion had been present, a surface
this scratched probably would not perform in quite the manner the
geometric model dictates.

Four other spheres suffered, to a lesser degree, from corrosion.
The 1.349 cm, 1.191 cm, and 0.873 cm spheres all fit into the same
category, with damage that is best considered mild. The fourth sphere,
0.556 cm in radius, has small local damage sites that all are located
within the same hemisphere. Careful positioning of the sphere before
each measurement eliminated their effect. All the spheres were examined
under the microscope; the smaller they were, the more difficult they
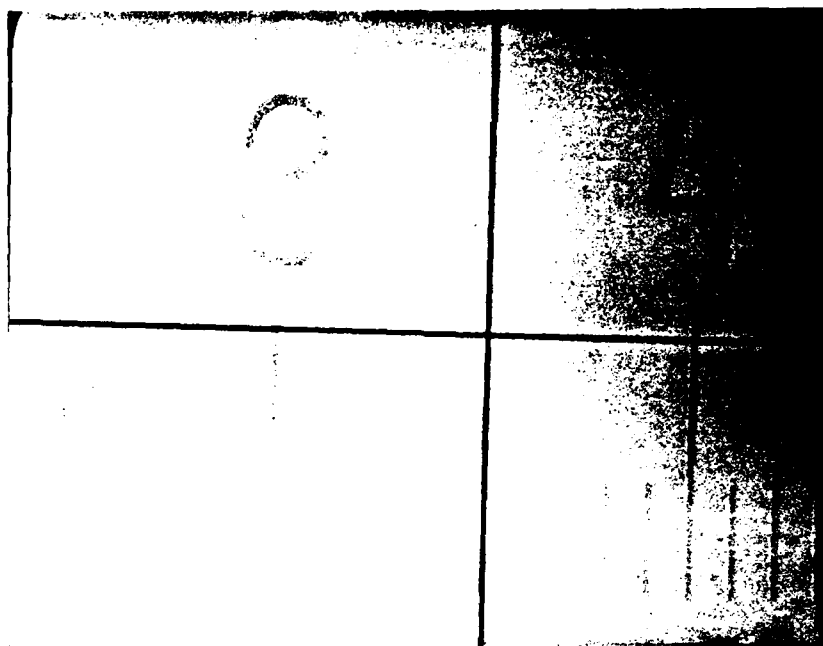were to properly photograph. Those which have not yet been mentioned in

Fig. 5.2. Linear Millimeter Scale (Magnified at ~57X)

this section have a good surface quality; coincidentally, they were never cleaned.

In Chapter IV (pg. 51), it was noted that as smaller and smaller spheres are supported by the same rod, the return signal from just that rod must increase. This effect can now be observed from the data in Table 5.15. The five largest ball bearings are each supported by the same lucite rod. Within that group, the rod's return signal size grows as the sphere's radius decreases. This group characteristic is true for all the rods. The reason that there is a discontinuity transitioning from one group to the next is that successive groups use smaller rods. Rod #1 is .0714 cm in diameter. Rod #2 is 0.397 cm in diameter. Rod #3 is 0.238 cm in diameter. Finally, Rod #4 is 0.119 cm in diameter.

The second page in Chapter III introduced the commonly accepted definition of the LRCS of a perfect specular sphere. Accordingly,

$$\sigma_L \text{ (SPHERE)} = \pi a^2$$

(9)

The practical use of such a sphere as a calibration standard implies that the measured return signal amplitude should vary primarily as a function of a^2. This will now be verified. Fig. 5.3 compares the theoretical linear relationship between σ_L and the return signal amplitude, with the actual measured values. The solid line in the figure represents the predicted relationship based on geometric theory, while the individual points represent the measured values. These values, although low, do tend to lie along a straight line provided that the data points representing the two largest and the two smallest spheres are disregarded. The predictions themselves may be high if the absorption within the collecting telescope is much more than the 2% assumed earlier. If, for instance, the absorption was 7.3%, the predicted line in Fig. 5.3 would sink to within 1% of six of the seven relevant data points. The errors associated with the four spheres that comprise both ends of the measurement scale can be explained. The two largest spheres have suffered noticeable surface damage. Although this is sufficient cause for disqualification of these spheres as serious calibration standards, surface corrosion alone might not properly account for the unexpectedly low signals measured from these two spheres. There is reason to suspect that the photodiode used for signal detection may have been operating in its non-linear regime when it outputted such large currents (displayed as voltage amplitudes) during the measurement of these two spheres. This possibility was not recognized until well after

77

the experiment had been concluded. The two smallest spheres are also plagued with a serious, but different, problem. Because of their miniature size, the lucite rod common to both should be replaced with a different support structure with an even lower LRCS. Because the smallest rod has a return signal of comparable size to the spheres, it is more difficult to accurately separate the two effects. Unfortunately, the size of the numeric values in this range are so small that even little errors can devastate the accuracy required of a calibration standard. It is therefore going to be recommended that such small spheres not be used as standards.
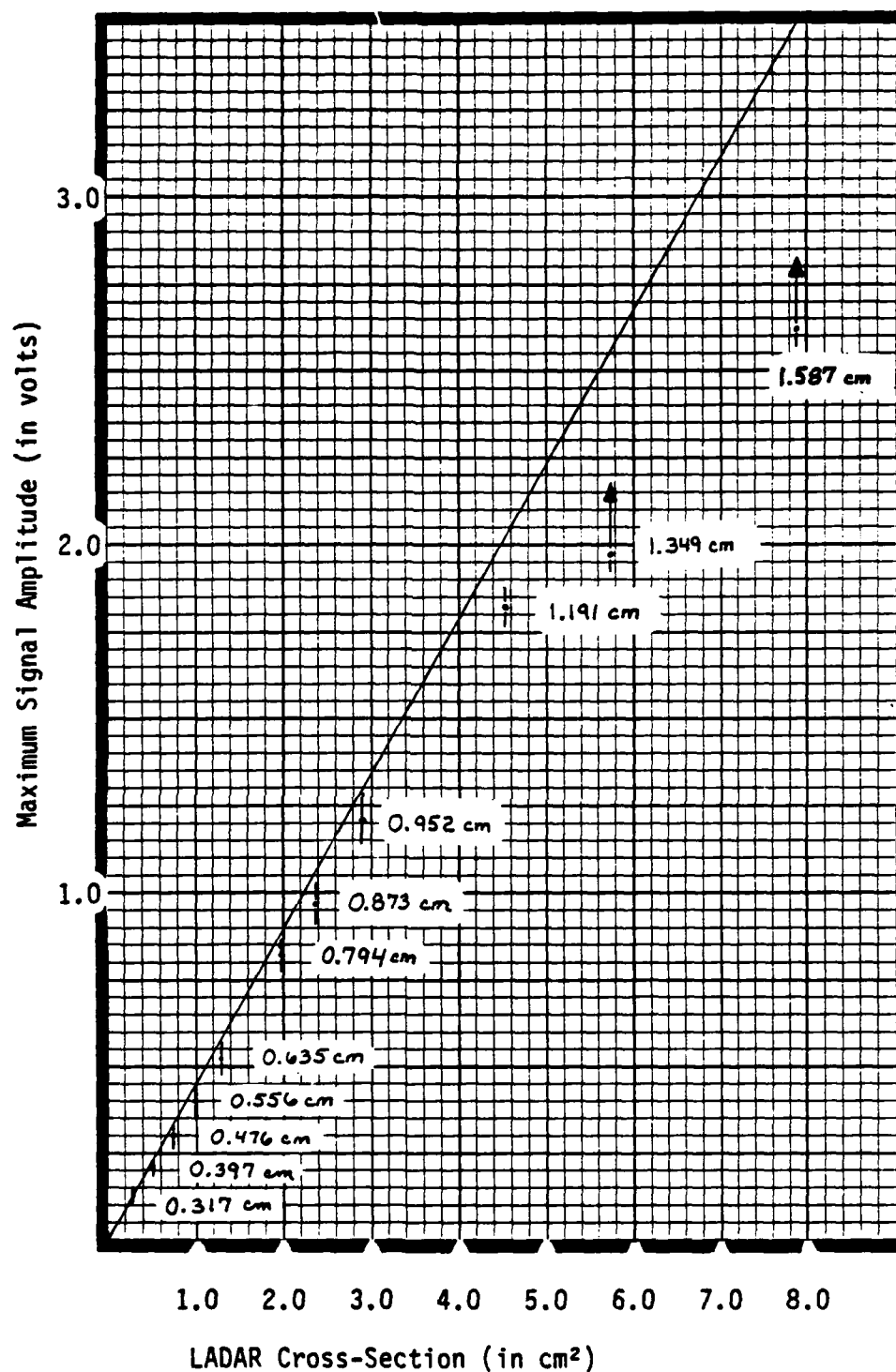
Fig. 5.3. Comparison of Predicted and Measured LRCS Values for the
Spherical Standards (each data point annotated with its
relevant sphere's radius)

VI. Conclusion

A LRCS Measurement Range has been designed and constructed to investigate the return signal from highly specular spheres. This was done according to the format presented in Chapter II. An analytic model of the experiment, based on geometric theory, was developed in Chapter III and its predictions were calculated. The laborious process of properly preparing the experimental set-up is critical to the accuracy of these absolute measurements. This preparatory process, and other useful error-reducing steps are reviewed in Chapter IV. The final LRCS measurements are presented in Chapter V, and an analysis of these results is performed within the context of the geometric model's predictions. This chapter capsulizes the important highlights and results of this research, and recommends areas for further study.

Discussion of the Research

The specular sphere can be an excellent standard for the calibration of a LRCS measurement range. However, much effort should first be dedicated to a thorough investigation of this standard's optical quality. Imperfections and inhomogeneties in the sphere may or may not affect the final results, but they will certainly increase the uncertainty assessed to the final data. Furthermore, sufficient effort should be invested to guarantee that the signal detector, chosen to perform these LRCS measurements, is operating within its linear region. Non-linear performance, unlike operation near the detector's saturation level, is not apparent from the temporal profile displayed on the CRT screen of the data collection equipment. In other words, great care

must be used to prevent this otherwise invisible error from being introduced to the final data.

The premier conclusion of this effort is that the maximum amplitude of the return optical signal from a sphere varies as a function of the square of the sphere's radius. This experimental data confirms that the universal definition for a sphere's LRCS (i.e., $\sigma_L = \pi a^2$) is valid, and, in fact, could just as correctly be replaced by any other function of a^2. Geometric Theory, within the limits of the experiment, has been shown to properly predict the amount of optical energy that can be expected at a detector after scattering from a specular sphere. The theory's dependence on very small angles is not as much a limitation as it is a warning that very tight tolerances on alignments will be required if accuracy is desired.

This measurement process has demonstrated both consistency and repeatability. An improved experimental version should include the necessary hardware to temporally measure a sample of the laser's outgoing wavefront. By monitoring the laser's performance during each run, greater accuracy will be achieved and fewer measurements will be required in order to properly interpret the results. Further recommendations include a suggestion that the experiment be re-designed to measure return signals from a sphere as a function of the bistatic angle, i.e., as a function of the detector's distance from the Nd:YAG laser's optic axis. This type of measurement might reveal that under certain conditions, the geometric optics model is insufficient. A different approach to the same problem would involve expanding on the work already done in Appendix C. The Huygens-Fresnel Theory has bee applied rigorously to the problem of scattering from a sphere. A

81

mathematical description of the reflectivity at every point on the sphere would be required. This description would have to account for phase changes on reflection, incident polarization of the laser beam, and the angle between the surface normal and the polarization vector. If this function were known, the backscattered intensity could then be calculated.

The measurement of a laser radar cross-section is a very difficult task. The interpretation of the results quickly becomes complicated if the target is other than a simple shape. Nonetheless, the simple shape is the building block upon which more complex target shapes are modeled. In much the same way, the sphere has proven itself. By virtue of its simplicity, it can be, if well cared for, an excellent standard for all other LRCS measurements.

Appendix A: Examination of the Relationship

Between r_0 and ρ

In Chapter III, small angle approximations were used to derive Eq (28), which is re-written below:

$$\rho = \frac{a r_0}{2 z_i - a} \tag{28b}$$

where

ρ = the normal distance between the z-axis and any point on the sphere

a = the sphere's radius

z_i = the distance between the sphere's center and the observation plane

r_0 = the normal distance between the z-axis and any point in the observation plane .

This linear relationship would be destroyed if the experiment considered values of r_0 which were much larger than ρ . This effect can be easily demonstrated. For values of z such that $a \geq z \geq \frac{a}{2}$,

$$\tan 2\theta \approx \frac{r_0 - \rho}{731.5} \tag{39}$$

$$2\theta \approx \tan^{-1}\left(\frac{r_0 - \rho}{731.5}\right) \tag{40}$$

$$\frac{d}{dr_0}(2\theta) \approx \frac{d}{dr_0}\left[\tan^{-1}\left(\frac{r_0 - \rho}{731.5}\right)\right] \tag{41}$$

83

$$2 \frac{d\theta}{dr_o} \approx \left[1 + \left(\frac{r_o - \rho}{731.5} \right)^2 \right]^{-1} (731.5)^{-1} \qquad (42)$$

Referencing Eq (22)

$$\theta = \sin^{-1} \left(\frac{\rho}{a} \right) \qquad (43)$$

$$\frac{d\theta}{dr_o} = \left(1 - \frac{\rho^2}{a^2} \right)^{-\frac{1}{2}} \frac{d}{dr_o} \left(\frac{\rho}{a} \right) \qquad (44)$$

$$= \left(a^2 - \rho^2 \right)^{-\frac{1}{2}} \frac{d\rho}{dr_o} \qquad (45)$$

Therefore, Eq (42) reduces to

$$\frac{d\rho}{dr_o} \approx \frac{\left(a^2 - \rho^2 \right)^{\frac{1}{2}}}{2 \left\{ 731.5 + \left[(r_o - \rho)^2 / 731.5 \right] \right\}} \qquad (46)$$

and

$$\frac{dr_o}{d\rho} \approx \frac{1463 + (r_o - \rho)^2 / (365.75)}{\left(a^2 - \rho^2 \right)^{\frac{1}{2}}} \qquad (47)$$

Eq (47) indicates that as ρ increases, the rate of growth of r_o increases even faster; this is because of the decreasing size of the denominator. It is only when r_o and ρ are of comparable size (i.e., when both have very small values) that $dr_o/d\rho$ is effectively constant. Within the context of Chapter III's discussion, it is when the derivative is no longer constant that the sphere's effective area deviates from a circle. The distortion occurs radially about the z-axis and would cause a

circular area (not centered on the z-axis) to become egg-shaped.

Appendix B: Signal Size Predictions for the 13 Test Spheres

Using the geometric optics model presented in Chapter III, the peak
amplitudes (in units of "volts") expected from each of the spheres can
be calculated. The energy measured by the photodiode (within its linear
operating region) is proportional to the magnitude of the signal it
emits; therefore, Eq (11) can be modified to read

$$V_{EXPECTED} = X A_{eff} \Gamma \eta T \tag{48}$$

where

> V_{EXP} = the voltage measured by the data collection equipment
>
> X = a convenient term for the measured energy density (in units
> of V/cm²)
>
> A_{eff} = effective surface area of the sphere, projected onto a
> plane, which re-radiates measured energy
>
> Γ = reflectivity of the sphere at 1.064 μm
> = .98
>
> η = round trip attenuation of the laser energy by the atmosphere
> = .99
>
> T = transmissivity of the telescope at 1.064 μm
> = .98

The evaluation of X is straight-forward. Fig. 2.5 plots the local
irradiance distribution within the flatter, central region of the
typical laser pulse. The maximum recorded magnitude is 23.0 Volts, and
it can be found in two separate regions almost 2 cm apart. The smallest
magnitude measured between these two peak regions is 20.0 Volts. In
order to maintain some analytical continuity across this region, all
points with magnitudes of 20.0 Volts or greater will be considered to be

part of the incident plane wave. The average of these 139 measurements is 21.01 Volts. When this data was accumulated, an attenuation filter was used to ensure a linear response from the photodiode. Because of it, the corrected average signal voltage is 175.08 V. This value represents the signal from an obscured detector; the .20 mm slit only exposes an active area of

$$(0.20 \text{ mm})(2.54 \text{ mm}) \approx .508 \text{ mm}^2 \tag{49}$$

Scaling this signal appropriately determines x :

$$x = \frac{175.08 \text{ V}}{.508 \text{ mm}^2} = 3.44 \times 10^2 \text{ V/mm}^2 \tag{50a}$$

$$x = 3.44 \times 10^4 \text{ V/cm}^2 \tag{50b}$$

The final calculation of $V_{expected}$ depends only on the computation for A_{eff} for each value of a, the sphere's radius. An example of this is presented in Chapter III by Eq (29a) through Eq (32). The results of this effort are listed in Table B.1.

Table B.1.

Signal Size Predictions

"a," the sphere's radius (cm)	A_{eff} (cm²)	$V_{expected}$ (volts)	(Millivolts)
1.587	1.076×10^{-4}	3.526	N/R*
1.349	7.774×10^{-5}	2.547	N/R*
1.191	6.061×10^{-5}	1.986	N/R*
0.952	3.874×10^{-5}	1.269	N/R*
0.873	3.258×10^{-5}	1.068	N/R*
0.794	2.695×10^{-5}	0.883	883.
0.635	1.724×10^{-5}	0.565	565.
0.556	1.322×10^{-5}	0.433	433.
0.476	9.691×10^{-6}	0.318	318.
0.397	$6.7\text{:}2 \times 10^{-6}$	0.221	221.
0.317	4.299×10^{-6}	0.141	141.
0.238	2.424×10^{-6}	0.079	79.
0.159	1.082×10^{-6}	0.036	36.

*. . . N/R = "Not Relevant"

Appendix C: Rigorous Application of Physical Optics

Using an analytic development somewhat similar to Erteza's (Erteza, 1981:1002-1007), the Huygen's-Fresnel principle can be expanded upon in order to calculate the local field amplitude for each individual point in the observation plane. By integrating over the telescope's entrance aperture, the total energy incident upon the detector can be calculated. The small angle approximations extensively relied on in Chapter 3 will not be used; to do so would be to deny the possible effects that points on the sphere, far from the optic axis, might have.

The plane wave of constant irradiance which is incident on the sphere is represented by

$$\tilde{u}(z) = A \exp\left[jk(z_i - z)\right] \tag{51}$$

where

   $\tilde{u}(z) =$ the complex amplitude of the field
   $A =$ the amplitude of the incident field
   $\quad =$ a constant
   $k =$ the wavenumber, $2\pi/\lambda$
   $z_i =$ the location of the observation plane along the z-axis
   $z =$ the axis along which the wavefront propagates

The irradiance of this field, measured in W/cm², is also a constant, I_0, and can be represented by

$$I_0 = |A|^2 \tag{52}$$

89

The problem is depicted in cylindrical coordinates in Fig. C.1. Breaking with standard convention, this incident wavefront will propagate from right to left, in the negative z-direction. The saving grace in this choice is the fact that, upon reflection, the scattered return field travels in the correct direction, from left to right, as tradition would have it. Every point $(\rho, \varnothing, z)$ on the illuminated portion of the sphere can be thought of as a point source whose contribution is weighted according to its distance from the z-axis. Using Gaskill's nomenclature, the complex amplitude of the backscattered field due to the point $(\rho, \varnothing, z)$ is

$$\tilde{u}'(\rho, \varnothing, z) = \eta\, \mathcal{R}(\theta, \varnothing)(\cos \theta)\, \tilde{u} \tag{53}$$

where
$$\tilde{u}'(\rho, \varnothing, z) = \tilde{u}'(z)$$

= . . . note: the "prime" indicates that reflection from the sphere has occurred.

η = the round trip attenuation of the laser pulse's energy by the atmosphere

$\mathcal{R}(\theta, \varnothing)$ = the reflectance of any specific point on the sphere's surface at $1.064\,\mu m$

$\cos \theta$ = an obliquity factor, or a form of "directional reflectivity"

(Gaskill, 1978:354). Both Goodman and Danielson also discuss the use of an obliquity factor as a "directivity pattern" for each secondary source (Goodman, 1968:42 Danielson, 1977:7). Because the incident plane wave is linearly polarized, the phase shifts arising upon reflection are not just functions of the angle of incidence, θ. "The phase shift occurs in
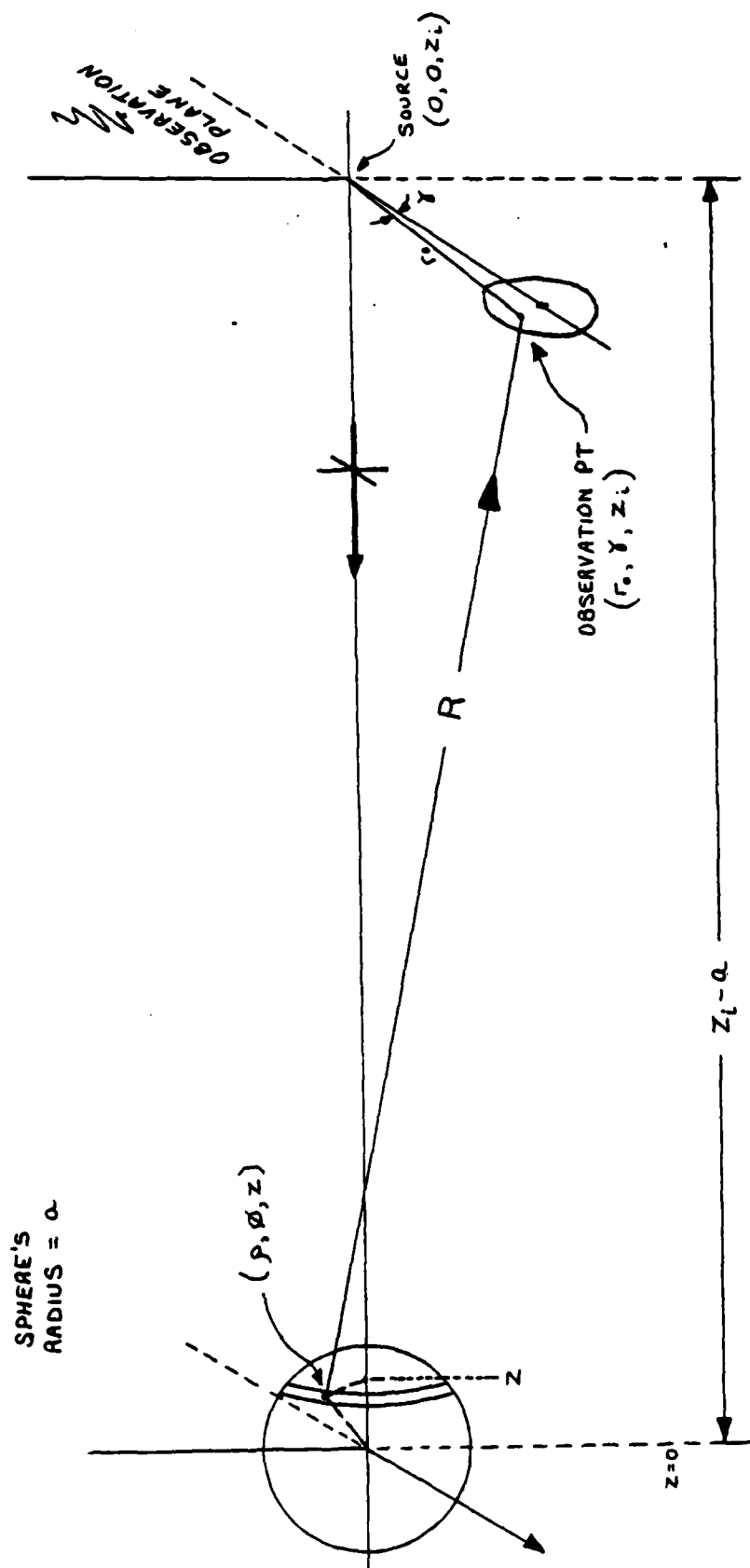
CYLINDRICAL COORDINATES

Fig. C.1. Three Dimensional Analysis of the Scattering Problem Within the Realm of Physical Optics

(not drawn to scale)

both components of the field (i.e., parallel and perpendicular to the plane of incidence," (Hecht and Zajac, 1979:89). Since the plane of incidence changes as a function of $\varnothing$, the phase shift must vary accordingly. The reflectance $\mathcal{R}$ of the metal therefore depends on both θ and $\varnothing$ (i.e., on the specific reflecting point on the sphere's surface). The term $\mathcal{R}$ will contain the phase shift and will remain unspecified throughout the rest of this development.

Rewriting Eq (53)

$$\tilde{u}'(z) = A \; \mathcal{R}(\theta,\varnothing) \; \eta \; \cos\theta \cdot \exp\left[jk(z_i - z)\right] \qquad (54)$$

Using the mathematical expression of the Huygens-Fresnel principle, the field amplititude (r_o , γ , z_i) can be determined (Goodman, 1968:58):

$$\tilde{u}'(r_o, \gamma, z_i) = \iint\limits_{SURFACE} h \cdot \tilde{u}'(\rho, \varnothing, z) \; dS \qquad (55a)$$

$$h = \frac{1}{j\lambda} \; \frac{\exp\left[jkR\right]}{R} \; \cos\left(\bar{n}, \bar{R}\right) \qquad (55b)$$

where

> h = a weighting function
> dS = a two-dimensional surface element at (ρ , $\varnothing$, z)
> $\bar{R}$ = the vector, assumed positive, which connects the surface point to the observation point
> $\bar{n}$ = the unit normal vector at (ρ , $\varnothing$, z)

Substituting Eq (54) and (55b) into Eq (55a):

$$\tilde{u}'(r_o, \gamma, z_i) = \iint\limits_{SURFACE} \frac{A \; \mathcal{R} \; \eta}{j\lambda \; R} \; \exp\left[jk(z_i - z) + jkR\right] \cos\theta \; \cos\left(\bar{n}, \bar{R}\right) \; dS$$

92

Referring to Fig. C.1, the following identities can be written:

$$\cos\theta = \frac{z}{a} \quad , \quad \longrightarrow \quad z = a\cos\theta \tag{56}$$

$$\sin\theta = \frac{\rho}{a} \quad , \quad \longrightarrow \quad \rho = a\sin\theta \tag{57}$$

Therefore

$$\tilde{u}'(r_o, \gamma, z_i) = \frac{A\eta}{j\lambda R}\iint\limits_{\text{SURFACE}} \exp\left[jkz_i - jka\cos\theta + jkR\right]$$

$$\times \quad \mathcal{R}(\theta,\varnothing)\cos\theta\,\cos(\bar{n},\bar{R})\,dS \tag{58}$$

Using the Fresnel approximation, i.e., that $R \approx Z_i$ when R is not multiplied by a very large factor (as it is in the exponent).

$$\tilde{u}'(r_o, \gamma, z_i) = \frac{A\eta}{j\lambda z_i}\iint \exp\left[jk(z_i - a\cos\theta) + jkR\right]$$

$$\times \quad \mathcal{R}(\theta,\varnothing)\cos\theta\,\cos(\bar{n},\bar{R})\,dS \tag{59}$$

But

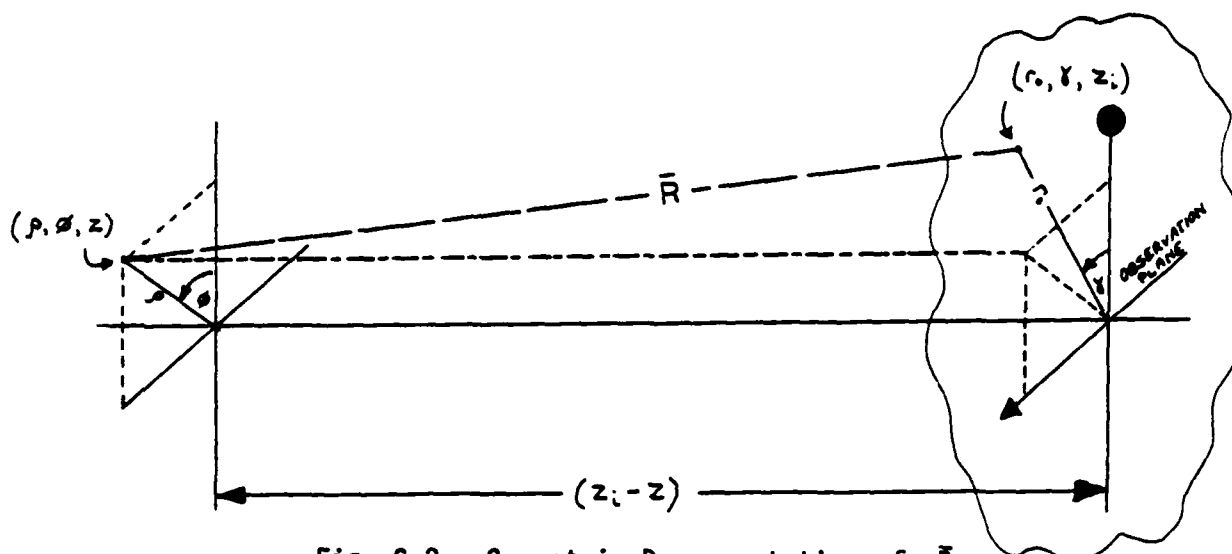$$dS = a\cos\theta\,d\theta\,\rho\,d\varnothing \tag{60a}$$

93

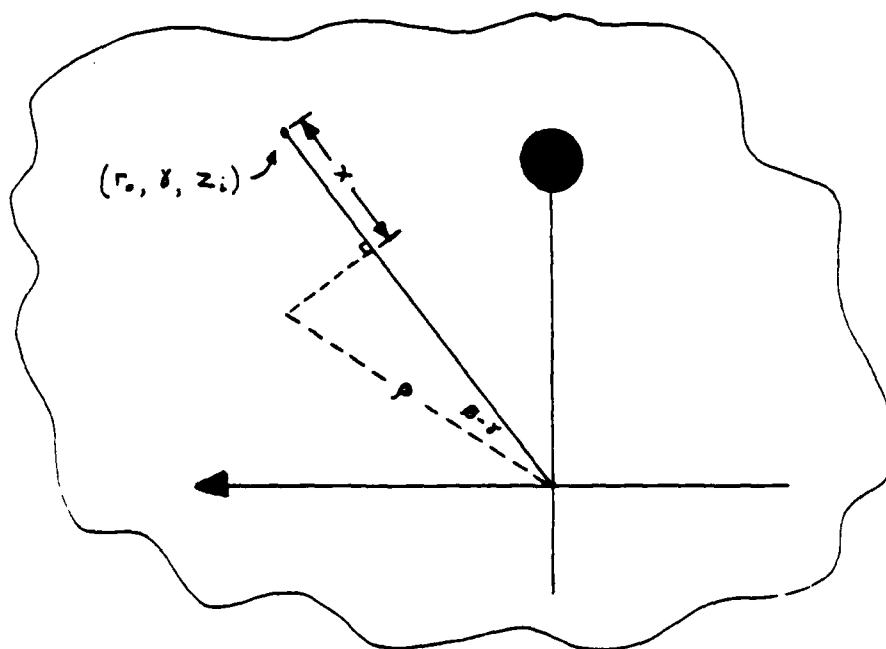Fig. C.2. Geometric Representation of $\bar{R}$

Fig. C.3. Enlargement of the Observation Plane Represented in Fig. C.2
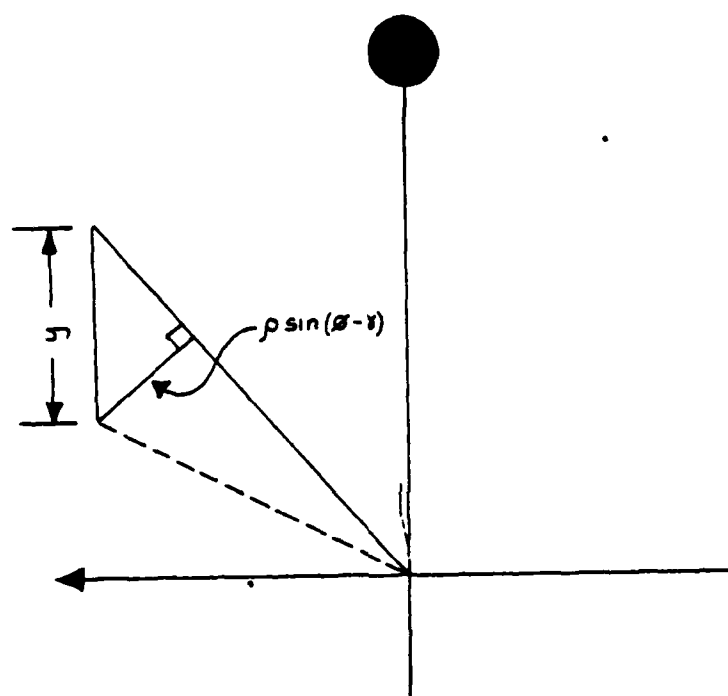
(not drawn to scale)

94

Fig. C.4   A Further Refinement of Fig. C.3

(not drawn to scale)

$$dS = a^2 \cos\theta \sin\theta \, d\theta \, d\phi \qquad (60b)$$

An exact geometric representation of R is still required. Solving in terms of the simple geometry of right triangles (see Figs. C.2-C.4), values of x and of y must first be determined. From Fig. C.3,

$$\cos(\phi - \gamma) = \frac{r_o - x}{\rho} \tag{61a}$$

$$r_o - x = \rho \cos(\phi - \gamma) \tag{61b}$$

$$x = r_o - \rho \cos(\phi - \gamma) \tag{61c}$$

Thus

$$y = \left[\rho^2 \sin^2(\phi-\gamma) + r_o^2 + \rho^2 \cos^2(\phi-\gamma) - 2r_o\rho\cos(\phi-\gamma)\right]^{1/2} \tag{62a}$$

$$y = \left[\rho^2 + r_o^2 - 2r_o\rho\cos(\phi-\gamma)\right]^{1/2} \tag{62b}$$

Finally, the geometric distance between the surface point and the observation point is determined by the right triangle which has R for a hypotenuse, and y and $(z-z_i)$ for legs.

$$R^2 = (z_i - z)^2 + \rho^2 + r_o^2 - 2r_o\rho\cos(\phi-\gamma) \tag{63}$$

It is here that the Fresnel approximation can be used. Re-writing R :

$$R = (z_i - z)\left\{1 + \frac{1}{(z_i-z)^2}\left[r_o^2 + \rho^2 - 2r_o\rho\cos(\phi-\gamma)\right]\right\}^{1/2} \tag{64a}$$

The allowed approximation is of the form

$$(1+b)^{\frac{1}{2}} \approx 1 + \frac{b}{2} \tag{64b}$$

provided that the next term in the series, $b^2/8$, is very small compared to unity. This can be readily verified by examining the maximum value of b under all of the worst conditions. These worst conditions include:

$$\cos 0^\circ = 1 \tag{65a}$$

$$r_o = 22 \tag{65b}$$

$$\rho = 2.7 \tag{65c}$$

$$z_i = 731.5 \tag{65d}$$

$$z = 2.7 \tag{65e}$$

$$(z_i - z)^{-2} = 1.9 \times 10^{-6} \tag{65f}$$

$$b_{MAX} = 7.0773 \times 10^{-4} \tag{65g}$$

The criteria for use of Eq (50b) is therefore met because

$$\frac{b^2}{8} = 5.0088 \times 10^{-7} \ll 1 \tag{65h}$$

Therefore

$$R \approx (z_i - z) \left\{ 1 + \frac{1}{2(z_i - z)^2} \left[r_o^2 + \rho^2 - 2 r_o \rho \cos(\phi - \gamma) \right] \right\} \tag{66a}$$

Because $(z - z_i) \approx z_i$

$$R \approx z_i - z + \frac{1}{2(z_i-z)}\left[r_o^2 + \rho^2 - 2r_o\rho\cos(\varnothing-\gamma)\right] \quad (66b)$$

becomes

$$R \approx z_i - z + \frac{1}{2z_i}\left[r_o^2 + \rho^2 - 2r_o\rho\cos(\varnothing-\gamma)\right] \quad (66c)$$

and

$$jkR \approx jk(z_i - a\cos\theta) + \left\{\frac{jk}{2z_i} \times \right.$$

$$\left. \left[r_o^2 + a^2\sin^2\theta - 2r_o(a\sin\theta)\cos(\varnothing-\gamma)\right]\right\} \quad (67)$$

Substituting Eq (61b) and (68) into Eq (60) yields

$$\tilde{u}' = \frac{A\ell}{j\lambda z_i} \int_o^{\pi/2} \int_o^{2\pi} a^2(\cos^2\theta)(\sin\theta)\left[\cos(\bar{n},\bar{R})\right] \times$$

$$R(\theta,\varnothing)\exp\left\{2jk(z_i - a\cos\theta)\right.$$

$$\left. + \frac{jk}{2z_i}\left[r_o^2 + a^2\sin^2\theta - 2ar_o\sin\theta\cos(\varnothing-\gamma)\right]\right\}d\varnothing\,d\theta \quad (68)$$

A new representation of $\cos(\bar{n},\bar{R})$ is necessary. The angle between $\bar{n}$ and $\bar{R}$ will now be referred to as β. The relationship between β and θ must be established so that the integration over $\varnothing$ and θ may be completed. In the coordinate system used to date, this problem would be three-dimensional. In order to simplify it to two-dimensions, the single plane containing both the vectors $\bar{n}$ and $\bar{R}$ (see Fig. C.5) must be identified. The three points that describe this plane are: (in
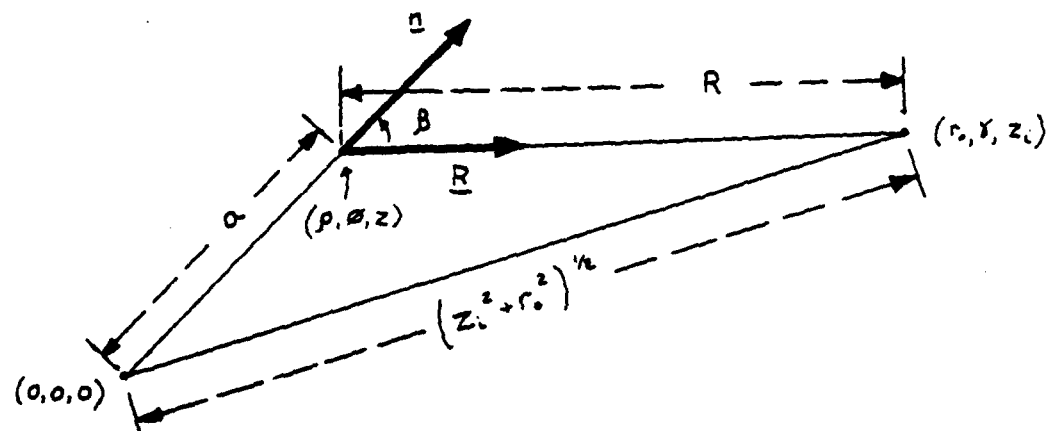
98

Fig. C.5. Geometry of the Plane Containing the Vectors $\underline{n}$ and

cylindrical coordinates), $(0,0,0)$, $(\rho,\varnothing,z)$, and (r_o,γ,z_i). Using the law of cosines, a relationship between each of the sides and the angle β can be written:

$$\left(z_i^2 + r_o^2\right) = \left(a\right)^2 + \left(R\right)^2 - 2\left(a\right)(R)\cos\left(\pi - \beta\right) \tag{69}$$

$$z_i^2 + r_o^2 - a^2 - R^2 = -2aR\cos\left(\pi - \beta\right) \tag{70a}$$

$$\frac{z_i^2 + r_o - a^2 - R^2}{2aR} = -\cos\left(\pi - \beta\right) \tag{70b}$$

but $\cos\left(\pi - \beta\right) = -\cos\beta$. Therefore

$$\frac{z_i^2 + r_o^2 - a^2 - R^2}{2aR} = \cos\beta \tag{71}$$

Manipulating Eqs (56) and (57), it can be shown that

$$z^2 + \rho^2 = a^2\cos^2\theta + a^2\sin^2\theta$$

99

$$z^2 + \rho^2 = a^2(\cos^2\theta + \sin^2\theta) = a^2 \tag{72}$$

Substituting Eqs (63) and (72), into Eq (71)

$$\cos\beta = \frac{z_i^2 + r_o^2 - a^2 - (z_i - z)^2 - \rho^2 - r_o^2 + 2r_o\rho\cos(\phi - \gamma)}{2aR} \tag{73a}$$

$$\cos\beta = \frac{z_i^2 - a^2 - z_i^2 + 2zz_i - (z^2 + \rho^2) + 2r_o\rho\cos(\phi - \gamma)}{2aR} \tag{73b}$$

$$\cos\beta = \frac{-2a^2 + 2zz_i + 2r_o\rho\cos(\phi - \gamma)}{2aR} \tag{73c}$$

Substituting Eq (66c) into the denominator

$$\cos\beta = -\frac{2a^2 - 2zz_i + \left[-2r_o\rho\cos(\phi - \gamma)\right]}{2a\left\{z_i - z + \frac{1}{2z_i}\left[r_o^2 + \rho^2 - 2r_o\rho\cos(\phi - \gamma)\right]\right\}} \tag{73d}$$

This substitution was made now so that the form of the denominator could be observed. Since no further manipulation of the terms in this substitution is expected, future equations will again refer to the denominator's bracketed term as R. The process of integration over ϕ will be greatly simplified if the cosine term containing ϕ can be eliminated from the numerator. This was the objective hidden in the substitution of an approximation for R in the denominator but not in the numerator. By manipulating the numerator so that it resembles the denominator, the cosine term in the numerator can be cancelled.

$$\cos\beta = -\frac{2a^2 - 2zz_i + \left[r_o^2 + \rho^2 - 2r_o\rho\cos(\phi-\gamma)\right] - r_o^2 - \rho^2}{2aR} \tag{74a}$$

$$= -\left(\frac{1/2z_i}{1/2z_i}\right)\left\{\frac{(2a^2 - 2zz_i - r_o^2 - \rho^2) + \left[r_o^2 + \rho^2 - 2r_o\rho\cos(\phi-\gamma)\right]}{2aR}\right\} \tag{74b}$$

$$= -\frac{(2z_i)^{-1}(2a^2 - 2zz_i - r_o^2 - \rho^2) + (2z_i)\left[r_o^2 + \rho^2 - 2r_o\rho\cos(\phi-\gamma)\right]}{(2z_i)^{-1}(2aR)} \tag{74c}$$

$$= -\frac{\left[(2z_i)^{-1}(2a^2 - 2zz_i - r_o^2 - \rho^2) - z_i + z\right] + R}{(2z_i)^{-1}(2aR)} \tag{74d}$$

$$= -\frac{(2z_i)^{-1}(2a^2 - 2zz_i - r_o^2 - \rho^2) - z_i + z}{(2z_i)^{-1}(2aR)} - \frac{R}{(2z_i)^{-1}(2aR)} \tag{74e}$$

$$= -\frac{\left[2a^2 - 2zz_i - r_o^2 - \rho^2 + 2z_i(z-z_i)\right]}{2aR} - \frac{z_i}{a} \tag{74f}$$

$$= \frac{2z_i^2 - 2a^2 + r_o^2 + \rho^2}{2aR} - \frac{z_i}{a} \tag{74g}$$

Substituting Eqs (56), (57), and (66c) into Eq (74g), the final form is

$$\cos\beta = \frac{2z_i^2 - 2a^2 + r_o^2 + a^2\sin^2\theta}{2a\left\{z_i - a\cos\theta + \frac{1}{2z_i}\left[r_o^2 + a^2\sin^2\theta - 2r_o a\sin\theta\cos(\phi-\gamma)\right]\right\}} - \frac{z_i}{a}$$
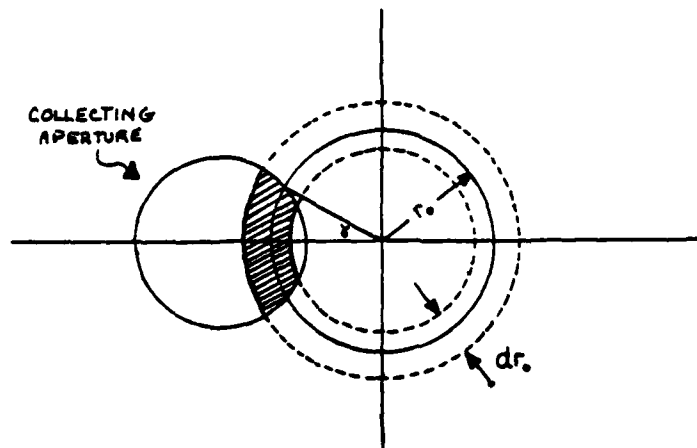
$$\tag{75}$$

101

Fig. C.6. Illustration of the Differential Area
Across Which $I(r_0)$ is Constant in the Plane $z=z_i$

Substituting Eq (75) into Eq (69) yields

$$\tilde{u}' = \frac{A\eta}{j\lambda z_i} a^2 \int_0^{\pi/2} \int_0^{2\pi} (\cos^2\theta)(\sin\theta)\, \mathcal{R}(\theta,\phi) \quad \times$$

$$\exp\left\{2jk(z_i - a\cos\theta) + \frac{jk}{2z_i}\left[r_0^2 + a^2\sin^2\theta - 2ar_0\sin\theta\cos(\phi-\gamma)\right]\right\} \quad \times$$

$$\left\{\frac{2z_i^2 - 2a^2 + r_0^2 + a^2\sin^2\theta}{2a\left\{z_i - a\cos\theta + (2z_i)^{-1}\left[r_0^2 + a^2\sin^2\theta - 2r_0 a\sin\theta\cos(\phi-\gamma)\right]\right\}}\right. \tag{76}$$

$$\left. - \frac{z_i}{a}\right\} d\phi\, d\theta$$

This double integral describes the complex field amplitude at the point
(r_0, γ, z_i). If the real part is then squared, the local irradiance is
then obtained. The total irradiance at the telescope's entrance can

102

then be calculated by integrating $\left|\tilde{u}'(r_\circ)\right|^2$ over the entrance aperture. Setting aside the problem of solving Eq (76), we will now address the question of integrating $\left|\tilde{u}'(r_\circ)\right|^2$ over the aperture.

Let $\left|\tilde{u}'(r_\circ)\right|^2 = I(r_\circ)$. $I(r_\circ)$ is a constant value for each of the points along the circumference of the circle of radius $r_\circ$. Since $I(r_\circ)$ is measured in units of watts per square centimeter, a differential area must be established over which the power can be calculated (see Fig. C.6). If γ were unbounded, then the differential area would be $2\pi r_\circ dr_\circ$. However, since only that differential area within the aperture is of interest, the modified area (the shaded portion in fig C.6) is just $2\gamma r_\circ dr_\circ$. Since γ has a different maximum value for every value of $r_\circ$ that connects with the collecting aperture's perimeter, a mathematical relationship must be established between these two terms. Using the law of cosines

$$b^2 = r_\circ^2 + c^2 - 2 r_\circ c \cos \gamma \qquad (77)$$

where

    b = radius of the aperture
       = 5.4 cm (constant)
    c = separation between the center of the aperture and the origin
       = 17 cm (constant)

Manipulating Eq (77)

$$\gamma = \cos^{-1}\left(\frac{r_\circ^2 + c^2 - b^2}{2 r_\circ c}\right) \qquad (78)$$

103

Thus, knowing the angular limits that define the collecting aperture, and knowing that r_0 is an extreme value at 17.0 ± 5.4 cm, an integral can be written which describes the power incident on the collecting telescope.

It is

$$P_{APERTURE} = \int_{11.6 \text{ cm}}^{22.4 \text{ cm}} 2\gamma r_0 \, I(r_0) \, dr_0 \qquad (79a)$$

$$= \int_{11.6 \text{ cm}}^{22.4 \text{ cm}} 2 r_0 \, I(r_0) \cos^{-1}\left(\frac{r_0^2 + c^2 - b^2}{2 r_0 c}\right) dr_0 \qquad (79b)$$

.

$$= 2 \int_{11.6 \text{ cm}}^{22.4 \text{ cm}} r_0 \, I(r_0) \cos^{-1}\left(\frac{r_0^2 + 259.8}{34 \, r_0}\right) dr_0 \qquad (79c)$$

When this power is known, a revised value at the detector can be estimated based on the expected absorptive losses in the telescope. Using Eq (34), the final signal size expected on the data collection equipment can be calculated.

104

BIBLIOGRAPHY

-----. "Theoretical Considerations of the Radar Equation," Technical Report AFAL-TR-75-116, Part 1. Air Force Armament Laboratory (AFSC), Eglin AFB, FL, 1975.

Bachman, Christian G. Laser Radar Systems and Techniques. Dedham, Mass: Artech House, Inc., 1979.

Born, Max and Emil Wolf. Principles of Optics. Oxford, England: Pergamon Press, 1970.

Danielson, B.L. Proposed Standards for Ladar Signatures. National Bureau of Standards, NBSIR 77-856, ADA038725. Washington D.C.: Government Printing Office, April 1977.

Demma, Fred and James Michels. Laser Radar Cross-Section and Reflectivity Measurements at .48, .63, and 10.6 Microns. Rome Air Development Center, RADC-TR-71-245, AD733345. Washington D.C.: Government Printing Office, November 1971.

D3013B-1. EG&G Electro-Optics. Data Sheet. Salem, Mass., July 1979.

Erteza, Ahmed. "Coherent Reflection of a Gaussian Beam at Optical Frequencies from a Large Convex Mirror." Journal of the Optical Society of America, 71: 1002-1007 (August 1981).

Gaskill, Jack D. Linear Systems, Fourier Tranforms, and Optics. New York: John Wiley and Sons, Inc., 1978.

Goodman, Joseph W. Introduction to Fourier Optics. San Francisco: McGraw-Hill Book Company, 1968.

Hecht, Eugene and Alfred Zajac. Optics. Reading, Mass.: Addison-Wesley Publishing Company, February 1979.

Henderson, G. and C. Weaver. "Determination of the Absolute Phase Change on Reflection at Chromium Films," Journal of the Optical Society of America, 54; 1052-1056 (August 1964).

Hengehold, Robert J. Lecture materials distributed in PHYS 642, Optical Diagnostics. School of Engineering, Air Force Institute of Technology (AV), Wright-Patterson AFB, OH, April 1985.

Hoover Universal, Inc. Technical Specifications Brochure. Ball and Roller Group, Cumming GA, 1983.

Huntley, Wright H., Jr. "New Coherent Light Diffraction Techniques," IEEE Spectrum: 114-122 (January 1964).

International Laser Systems. Operation, Maintenance, and Service Instructions for Laboratory Laser Systems. User Manual. ILS, Orlando, 1979.

Jenkins, Francis A. and Harvey E. White. Fundamentals of Optics. New York: McGraw-Hill Book Company, 1976.

Kerker, Milton. "Light Scattering from Colloidal Spheres and Cylinders," Proceedings of the Second Interdisciplinary Conference on Electromagnetic Scattering. 55-98. Gordon and Breach Science Publishers, New York, 1965.

Marcuse, Dietrick. Light Transmission Optics. New York: Van Norstrand Reinhold Company, 1972.

Mills, James P. Lecture materials distributed in PHYS 544, Fundamentals of Optics III. School of Engineering, Air Force Institute of Technology (AV), Wright-Patterson AFB, OH, April 1985.

National Bureau of Standards. Tables of Scattering Functions for Spherical Particles, Forward by Julius A. Stratton. Applied Mathematics Series-4. Washington, D.C.: Government Printing Office, 1948.

Optical Society of America. Handbook of Optics, New York: McGraw-Hill Book Company, 1978.

Schefter, Jim. "Invisible Bomber--Secrets of the Plane that RADAR Can't See," Popular Science: 60-63 (February 1983).

Skolnik, Merrill I. Introduction to Radar Systems. New York: McGraw-Hill Book Company, 1962.

Stratton, Julius A. Electromagnetic Theory. New York and London: McGraw-Hill Book Company, 1941.

Tektronix. 7834 Storage Oscilloscope. Instruction Manual. Tektronix, Inc., Beaverton, Oregon, 1983.

U.S. Precision Lens. The Handbook of Plastic Optics. Cincinnati: U.S. Precision Lens Inc., 1973.

Wyman, Paul W. "Definition of Laser Radar Cross-Section," Applied Optics, 7: 207 (January 1968).

Wyman, Paul W. Laser Radar Range Equation Considerations. Naval Research Laboratory, AD 699 519. Washington D.C.: Government Printing Office, December 1969.

VITA

Captain James C. Higgins was born on 22 July 1958 in Miami, Florida. He graduated from high school in 1976 and attended the University of Notre Dame from which he received the degree of Bachelor of Science in Physics in May 1980. Upon graduation, he received a commission in the United States Air Force through the ROTC program. His first assignment was to the Air Force Weapons Laboratory, Kirtland AFB, New Mexico. While there, he served as an optical physicist for, and a flight crew member on, the Airborne Laser Laboratory. In November 1982, he met Kathy Klattenhoff and in May 1984, they were married. Following the honeymoon, he entered the School of Engineering, Air Force Institute of Technology.

Permanent address: 3781 S.W. 27 Lane

Miami, Florida 33134

107

AD-A163 955

REPORT DOCUMENTATION PAGE

1a. REPORT SECURITY CLASSIFICATION UNCLASSIFIED	1b. RESTRICTIVE MARKINGS
2a. SECURITY CLASSIFICATION AUTHORITY	3. DISTRIBUTION/AVAILABILITY OF REPORT
2b. DECLASSIFICATION/DOWNGRADING SCHEDULE	Approved for public release; distribution unlimited.
4. PERFORMING ORGANIZATION REPORT NUMBER(S) AFIT/GEP/ENP/85D-5	5. MONITORING ORGANIZATION REPORT NUMBER(S)

6a. NAME OF PERFORMING ORGANIZATION School of Engineering	6b. OFFICE SYMBOL (If applicable) AFIT/EN	7a. NAME OF MONITORING ORGANIZATION
6c. ADDRESS (City, State and ZIP Code) Air Force Institute of Technology Wright-Patterson AFB, Ohio 45433		7b. ADDRESS (City, State and ZIP Code)
8a. NAME OF FUNDING/SPONSORING ORGANIZATION	8b. OFFICE SYMBOL (If applicable)	9. PROCUREMENT INSTRUMENT IDENTIFICATION NUMBER

8c. ADDRESS (City, State and ZIP Code)	10. SOURCE OF FUNDING NOS.			
	PROGRAM ELEMENT NO.	PROJECT NO.	TASK NO.	WORK UNIT NO.

11. TITLE (Include Security Classification) See Box 19

12. PERSONAL AUTHOR(S) James C. Higgins, B.S., Capt, USAF

13a. TYPE OF REPORT MS Thesis	13b. TIME COVERED FROM _____ TO _____	14. DATE OF REPORT (Yr., Mo., Day) 1985 December	15. PAGE COUNT 108

16. SUPPLEMENTARY NOTATION

17. COSATI CODES			18. SUBJECT TERMS (Continue on reverse if necessary and identify by block number)
FIELD	GROUP	SUB. GR.	Optical Radar, Infrared Detection
14	02		
17	08		

19. ABSTRACT (Continue on reverse if necessary and identify by block number)

Title: THE CONSTRUCTION AND CALIBRATION OF A LADAR CROSS-SECTION MEASUREMENT RANGE

Approved for public release: IAW AFR 190-1.
JOHN E. WOLAVER   16 JAN 86
Dean for Research and Professional Development
Air Force Institute of Technology (ATC)
Wright-Patterson AFB OH 45433

Thesis Chairman: James P. Mills, Major, USAF

20. DISTRIBUTION/AVAILABILITY OF ABSTRACT UNCLASSIFIED/UNLIMITED ⊠ SAME AS RPT. ☐ DTIC USERS ☐	21. ABSTRACT SECURITY CLASSIFICATION UNCLASSIFIED
22a. NAME OF RESPONSIBLE INDIVIDUAL James P. Mills, Major, USAF	22b. TELEPHONE NUMBER (Include Area Code) 513-255-2012	22c. OFFICE SYMBOL AFIT/PH

DD FORM 1473, 83 APR   EDITION OF 1 JAN 73 IS OBSOLETE.

This research effort measured the size of the optical signals scattered by highly specular spheres when illuminated by plane wavefronts. This was repeated for 13 different sized spheres so that the functional dependency on sphere size could be more accurately established. The experiment was conducted at $\lambda = 1.064\,\mu m$ and at a fixed range of 731.5 cm in a bistatic configuration.

An analytical development based on geometric optics was used to predict the results. Within the limits of the small angle approximations, the results were generally within 10% of the measured values. The surface quality of the spheres and the alignment of the experiment were found to be the most critical variables affecting accuracy.